**ORIGINAL ARTICLE**

WILEY    *Journal of* METAMORPHIC GEOLOGY

# Influence of dissolution/reprecipitation reactions on metamorphic greenschist to amphibolite facies mica $^{40}Ar/^{39}Ar$ ages in the Longmen Shan (eastern Tibet)

Laura Airaghi[1]  iD  |  Clare J. Warren[2]  |  Julia de Sigoyer[1]  |  Pierre Lanari[3]  |
Valérie Magnin[1]

[1]CNRS, ISTerre, Université Grenoble
Alpes, Grenoble, France

[2]School of Environment, Earth and
Ecosystem Sciences, The Open
University, Milton Keynes, UK

[3]Institute of Geological Sciences,
University of Bern, Bern, Switzerland

**Correspondence**
Laura Airaghi, Sorbonne Université,
ISTeP, 4 place Jussieu 75005 Paris,
France.
Email: laura.airaghi@upmc.fr

**Present address**
Laura Airaghi, Sorbonne Université,
CNRS,Institut des Sciences de la Terre de
Paris (ISTeP), Paris, France.

**Abstract**

Linking ages to metamorphic stages in rocks that have experienced low- to medium-grade metamorphism can be particularly tricky due to the rarity of index minerals and the preservation of mineral or compositional relicts. The timing of metamorphism and the Mesozoic exhumation of the metasedimentary units and crystalline basement that form the internal part of the Longmen Shan (eastern Tibet, Sichuan, China), are, for these reasons, still largely unconstrained, but crucial for understanding the regional tectonic evolution of eastern Tibet. In situ core-rim $^{40}Ar/^{39}Ar$ biotite and U–Th/Pb allanite data show that amphibolite facies conditions (~10–11 kbar, 530°C to 6–7 kbar, 580°C) were reached at 210–180 Ma and that biotite records crystallization, rather than cooling, ages. These conditions are mainly recorded in the metasedimentary cover. The $^{40}Ar/^{39}Ar$ ages obtained from matrix muscovite that partially re-equilibrated during the post peak-*P* metamorphic history comprise a mixture of ages between that of early prograde muscovite relicts and the timing of late muscovite recrystallization at *c.* 140–120 Ma. This event marks a previously poorly documented greenschist facies metamorphic overprint. This latest stage is also recorded in the crystalline basement, and defines the timing of the greenschist overprint (7 ± 1 kbar, 370 ± 35°C). Numerical models of Ar diffusion show that the difference between $^{40}Ar/^{39}Ar$ biotite and muscovite ages cannot be explained by a slow and protracted cooling in an open system. The model and petrological results rather suggest that biotite and muscovite experienced different Ar retention and resetting histories. The Ar record in mica of the studied low- to medium-grade rocks seems to be mainly controlled by dissolution–reprecipitation processes rather than by diffusive loss, and by different microstructural positions in the sample. Together, our data show that the metasedimentary cover was thickened and cooled independently from the basement prior to *c.* 140 Ma (with a relatively fast cooling at 4.5 ± 0.5°C/Ma between 185 and 140 Ma). Since the Lower Cretaceous, the metasedimentary cover and the crystalline basement experienced a coherent history during which both were partially exhumed. The Mesozoic history of the Eastern border of the Tibetan plateau is therefore complex and polyphase, and the

basement was actively involved at least since the Early Cretaceous, changing our perspective on the contribution of the Cenozoic geology.

# 1 | INTRODUCTION

One of the major contributions to the understanding of the tectonic evolution of orogenic belts is the quantification of the rates of different parts of the burial and exhumation cycle experienced by the rocks now cropping out at the surface (e.g. Spear & Parrish, 1996; Hermann & Rubatto, 2003; Janots et al., 2009). However, in low- to medium-grade metamorphic terranes that have experienced multiple stages of metamorphism, distinguishing between, and dating, the different metamorphic event(s) can be challenging. Difficulties mainly derive from the significant mineral, compositional and microstructural inheritance preserved in the samples at relatively low temperatures.

Modern analytical instrumentation allows the structural complexity and chemical heterogeneity of low-grade metamorphic minerals to be imaged and quantified with high precision (at the scale of 1–10 μm), especially in mica-bearing systems (e.g. Lanari et al., 2012, 2013; Lanari, Vidal, et al., 2014; Scheffer et al., 2016). In such systems, $^{40}$Ar/$^{39}$Ar dating of mica is commonly used to determine the timing of metamorphic cooling following the traditional interpretation of Dodson's diffusion theory (Dodson, 1973), due to the ubiquity of mica and its importance as a geobarometer. However, the concentration of Ar incorporated in, or lost from a grain, is not only dependent on the cooling history and the grain size (as suggested by the Dodson, 1973 formulation) but also on the effectiveness of the grain boundary fluid network in removing Ar (the "openness" of the system) and the variation of the rates of fluid-induced replacement mineral reactions (Cenki-Tok, Darling, Rolland, Dhuime, & Storey, 2014; de Sigoyer et al., 2000; Di Vincenzo, Ghiribelli, Giorgetti, & Palmeri, 2001; Fornash, Cosca, & Whitney, 2016; Mulch & Cosca, 2004; Villa, 2010, 2016; Warren, Hanke, & Kelley, 2012; Warren, Smye, Kelley, & Sherlock, 2012).

Therefore, since many tectonic time-scale estimates rely on the interpretation of metamorphic ages (Lanari, Rolland, et al., 2014; Sanchez et al., 2011) and associated cooling rates (e.g. Mulch, Cosca, Andersen, & Fiebig, 2005; Rolland, Sosson, Adamia, & Sadradze, 2011), an integrated petrological and geochronological approach is necessary to precisely assess age significance within the geological context (Allaz, Engi, Berger, & Villa, 2011; Villa, 2016; Villa,

Bucher, Bousquet, Kleinhanns, & Schmid, 2014). In complex cases, $^{40}$Ar/$^{39}$Ar data may be combined with data from independent geochronometers (e.g. U–Th/Pb on zircon, monazite and allanite) and with results from numerical diffusion models to provide a means for distinguishing whether Ar age variations derive purely from Ar diffusion—thus providing constraints on cooling rates—or whether they derive from mineral recrystallization reactions during metamorphism (Cenki-Tok et al., 2014; Mulch & Cosca, 2004).

In the low- to medium-grade metamorphic rocks of the central Longmen Shan (eastern Tibetan plateau, Figure 1), petrological studies have documented a complex pattern of chemical heterogeneities within the metamorphic minerals, in particular within matrix white mica, relating to different phases of deformation and chemical re-equilibration events (Airaghi, Lanari, de Sigoyer, & Guillot, 2017; Airaghi, de Sigoyer, et al., 2017; Worley & Wilson, 1996). Field structures provide evidence for two successive compressional events: the first linked to the Late Triassic–Early Jurassic orogeny related to the closure of the Paleotethys, and coeval with granite emplacement from 224 to 188 Ma (Chen & Wilson, 1995; de Sigoyer, Vanderhaeghe, Duchene, & Billerot, 2014; Harrowfield & Wilson, 2005; Roger, Jolivet, & Malavieille, 2010; Roger, Malavieille, Leloup, Calassou, & Xu, 2004; Yan, Zhou, Li, & Wei, 2011); and the second linked to the Cenozoic reactivation starting in the Eocene after the India–Asia collision (e.g. Arne et al., 1997; Wang et al., 2012). This latter event includes a period of rapid exhumation of the Longmen Shan crystalline units from *c.* 10 Ma, as demonstrated by U–Th/He apatite and zircon fission track ages (Godard et al., 2009; Kirby et al., 2002; Li, Currie, Rowley, & Ingalls, 2015; Li et al., 2012; Richardson et al., 2008; Tan, Lee, Xu, & Cook, 2017; Wang et al., 2012). A period of tectonic quiescence and slow cooling at rates of ~1°C/Ma has been proposed between the two deformation phases (e.g. Roger, Jolivet, Cattin, & Malavieille, 2011). This suggestion was recently called into question by new $^{40}$Ar/$^{39}$Ar ages that appear to document the reactivation of the crystalline Pengguan massif under greenschist facies conditions at *c.* 137 Ma, during the Early Cretaceous (Airaghi, de Sigoyer, et al., 2017).

In the internal domain of the belt (the area located west of the Wenchuan fault, WF in Figure 1a–c), rocks record three stages of a clockwise metamorphic path: two stages
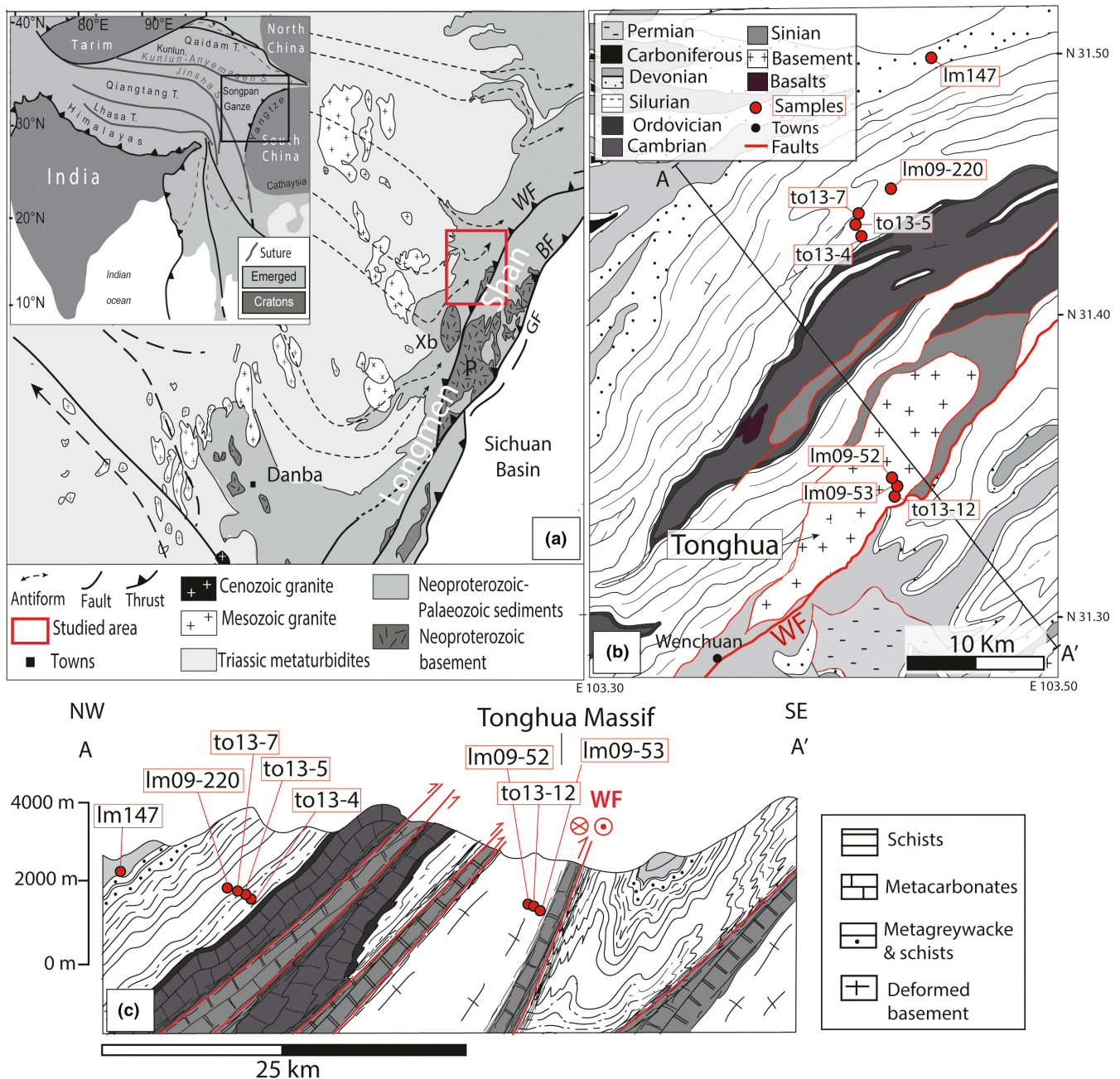
**FIGURE 1** (a) Simplified geological and structural maps of eastern Tibet, modified from Billerot et al. (2017). The inset indicates the location of the Longmen Shan within Asia. Xb = Xuelongbao massif; P = Pengguan massif; WF = Wenchuan fault; BF = Beichuan fault; GF = Guanxian fault. (b) Geological map of the studied area. Sample locations are indicated by red dots. The black line defines the profile of the cross-section in panel (c). (c) Geological cross-section along the profile AA'. The location of the studied samples is projected on the section (red dots)

of amphibolite facies metamorphism related to the thickening of the sedimentary series and to the beginning of their exhumation (Airaghi, Lanari, et al., 2017; Worley & Wilson, 1996). These stages are also observed in the Danba area (southeast of the Longmen Shan) at higher metamorphic conditions (Billerot, Duchene, Vanderhaeghe, & de Sigoyer, 2017; Huang, Maas, Buick, & Williams, 2003; Jolivet, Roger, Xu, Paquette, & Cao, 2015; Weller et al., 2013). Amphibolite facies metamorphism was then

followed by a greenschist facies overprint (Airaghi, Lanari, et al., 2017; Dirks, Wilson, Chen, Luo, & Liu, 1994). This complex tectono-metamorphic history and the relatively low metamorphic grade of the rocks make the geochronological estimations of the different metamorphic events particularly challenging. In situ U–Pb monazite ages obtained from the metasedimentary cover in the Danba area (Figure 1a) bracket the medium-grade metamorphic history between 190 and 180 Ma (e.g. Weller et al., 2013). In the

Longmen Shan, whether major metamorphic minerals, such as biotite and muscovite, used for thermobarometric estimates record similar metamorphic events still remains largely unconstrained. The timing and conditions of the greenschist facies overprint are also still unclear. In this study, we report a new data set of in situ metamorphic biotite and muscovite $^{40}Ar/^{39}Ar$ ages for the internal domain of the Longmen Shan (Figure 1b,c) to provide the first petrochronological set of data for the belt and to date the greenschist overprint.

In situ $^{40}Ar/^{39}Ar$ dating was carried to ensure the best spatial resolution possible in order to date minerals in different microstructural sites. Considering their close chemical composition, it would not be easy to discriminate between mica generations by standard step heating techniques. In order to strengthen age interpretation and decipher the major process controlling the $^{40}Ar/^{39}Ar$ record, in situ dating was combined with (1) previously reported and newly acquired compositional mapping, microstructural observations and P–T paths to put ages into a petro-structural context; (2) allanite (REE-rich epidote) U–Th/Pb ages used as an independent chronometer; and (3) simple diffusion models to explore the effect of different cooling paths and rates on $^{40}Ar/^{39}Ar$ ages.

This study provides new time constraints on the timescales of metamorphic processes in the internal domain of the central Longmen Shan and in eastern Tibet in general during the Mesozoic, revealing a previously poorly documented Early Cretaceous phase. Furthermore, our results provide important insights into the petrological processes that control different $^{40}Ar/^{39}Ar$ signatures in muscovite and biotite in low- to medium-grade metamorphic samples.

## 2 | GEOLOGICAL SETTING

The Longmen Shan range is located at the eastern border of the Tibetan plateau, between the Songpan-Ganze block to the west and the Sichuan basin (South China Craton) to the east (Figure 1a). From east to west (from the frontal to the internal part of the belt), three faults strike parallel to the belt: the Guanxian, the Beichuan and the Wenchuan

faults. This last one lies in the ductile Wenchuan Shear Zone (Figure 1a). The Neoproterozoic South China Craton crops out in the Pengguan and Xuelongbao crystalline massifs, in the hangingwall of the Beichuan and Wenchuan faults respectively (Yan et al., 2008; Zhou, Yan, Wang, Qi, & Kennedy, 2006). In the hangingwall of the Wenchuan fault, the Tonghua crystalline massif also crops out as a 75 km long slice of metagranitic and metagranodioritic rocks (Figure 1b,c) and is considered here to also belong to the South China Craton, due to its petrological characteristics and its association with the Neoproterozoic sedimentary roof ("Sinian" in Figure 1b).

The Tonghua massif is bounded to the northeast by a tectonic contact that separates it from the medium-grade metamorphosed Palaeozoic–Mesozoic sedimentary cover, structurally above the basement (Figure 1b,c). The metasedimentary cover mainly includes deformed Silurian metapelites and Devonian metagreywackes. The Tonghua massif is folded, as demonstrated by the occurrence of the Neoproterozoic (Sinian) sedimentary rocks at both sides of the massif (Figure 1b,c). Close to the Wenchuan fault, the crystalline rocks are deformed under brittle–ductile conditions. Deformation is defined by northwest-dipping cleavage, cm-scale shear zones and veins where the basement is metamorphosed under greenschist facies conditions, with assemblages of chlorite+white mica+epidote+quartz.

In the Tonghua and Pengguan crystalline massifs, the greenschist facies metamorphism is the major metamorphic overprint observed. No clear evidence of a higher grade metamorphic history has been identified, in agreement with petrological observations on other crystalline massifs in the belt (e.g. Airaghi, de Sigoyer, et al., 2017). In the sedimentary cover of the Tonghua massif, an amphibolite facies assemblage characterized by garnet and biotite (±allanite) has been overprinted by a later greenschist assemblage (Airaghi, Lanari, et al., 2017; Dirks et al., 1994; Worley & Wilson, 1996). The geographical proximity of these different metamorphic domains poses questions regarding the timing of their juxtaposition as well as the difference between the metamorphic conditions of the metasedimentary cover and the

**FIGURE 2** Photomicrographs of studied metapelites. Mineral abbreviations are from Whitney and Bernard (2010) except for white mica = Wm. (a) Interpretative sketch of the microstructural and mineral evolution of the studied samples. (b) Plane polarized light (PPL) image of deformed biotite porphyroblast and the S1 and S2 Wm-bearing cleavage (red and blue) in sample to13-4. At biotite rims, Wm+Chl develop (dashed green line). (c) Backscattered electron (BSE) image showing the geometric relations between the crenulated S1 Chl+Wm cleavage (red) and the S2 Wm-bearing cleavages (with minor chlorite, blue) in sample to13-4. (d) BSE image of a biotite porphyroblast in sample to13-4 with its incipient Wm+Chl pressure shadows (dashed green lines), modified from Airaghi, Lanari, et al. (2017). (e) PPL image of biotite porphyroblasts in sample to13-5 overgrowing the main cleavage. Late, narrow white mica flakes superimpose the biotite grain. (f) BSE image of garnet and biotite porphyroblasts in sample to13-5. (g) BSE image of garnet in sample to13-7, recording both S1 and S2 in inclusion trails. (h) PPL image of sample lm147. The deformed porphyroclast is made of Qz+Fe-oxide (pseudomorphing an early allochtonous clast). The inset shows an enlarged view of the S1 cleavage (red) preserved within S2 domains (underlined in blue)
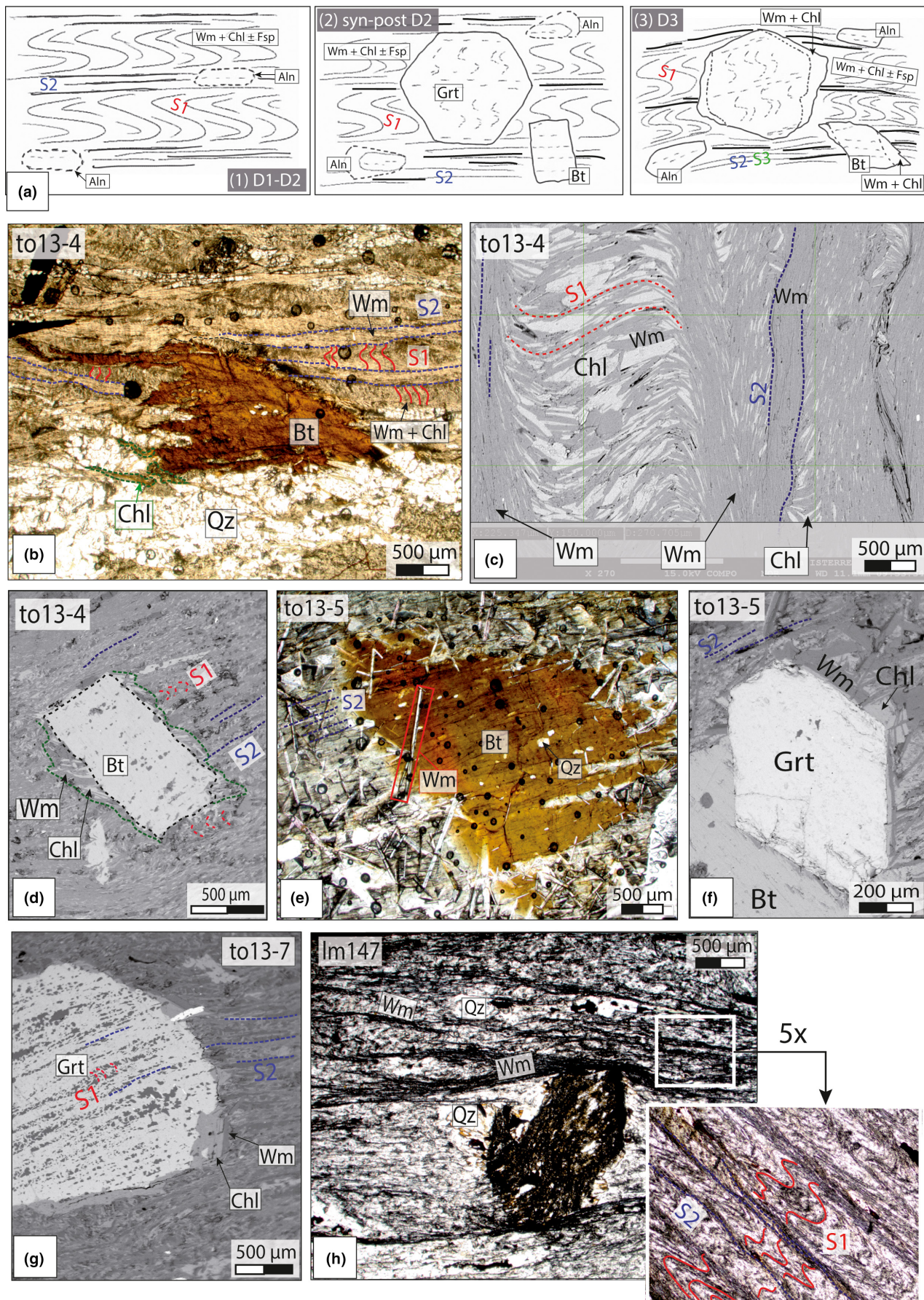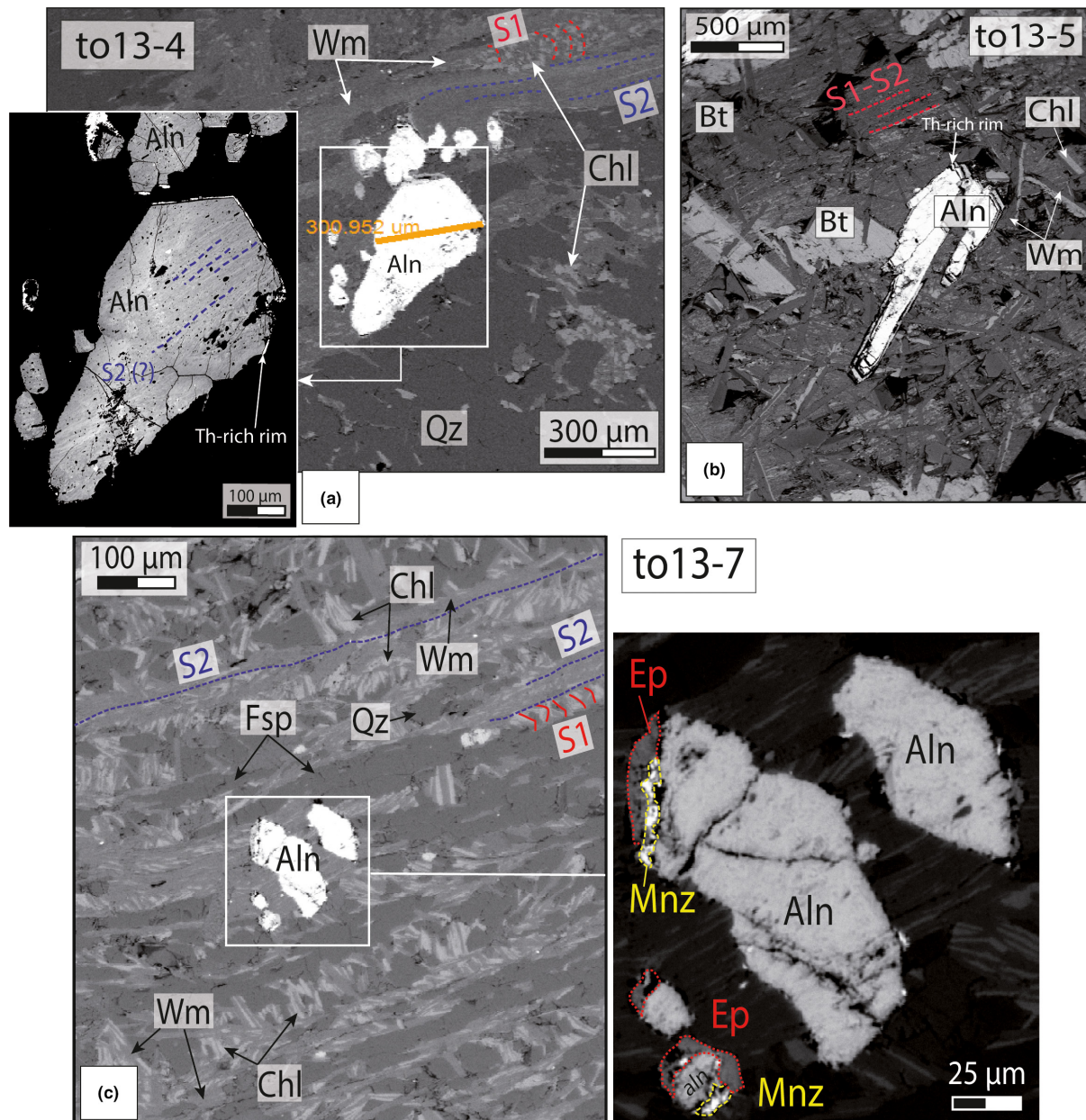
**FIGURE 3** (a) BSE image of allanite porphyroblasts aligned with, and partly overgrowing, the S2 cleavage (blue dashed line) in sample to13-4. (b) Allanite overgrowing the main cleavage in sample to13-5. (c) BSE image of allanite grains overprinting the S1–S2 cleavage in sample to13-7. Allanite is surrounded by a Mnz+Ep rims as shown in the enlarged view on the right

crystalline massifs. For this study, a series of samples was collected: (1) in the lower structural levels of the pelitic metasedimentary cover exhumed in the hanging-wall of the WF at a similar distance from the WF (samples to13-4, to13-5, to13-7 and lm09-220 of Figures 1b, 2 and 3); (2) in the upper crustal level of the same series (sample lm147) 35 km northeast from the WF; and (3) in the Tonghua crystalline massif, close to the WF (samples lm09-52, lm09-53 and to13-12 of Figures 1b, 3 and 4, see also Table 1 for sample location), in order to identify possible differences in the petrochronological evolutions of different units.

# 3 | SAMPLE DESCRIPTION AND THERMOBAROMETRY

## 3.1 | Methods

Major minerals and allanite grains were identified on polished thin sections using optical microscopy and in back-scattered electron images obtained using a scanning electron microscope S2500 Hitachi at Institut des Sciences de la Terre (ISTerre—University Grenoble Alps, France; Figures 2–4). The chemistry of the major minerals was analysed with an electron microprobe analyser (EMPA)

**TABLE 1** Location and physical conditions of the samples

| Sample name | Longitude | Latitude | Lithology | $T_{peak}$ conditions (°C) | Method used |
|---|---|---|---|---|---|
| to13-4 | E103.682310 | N31.720520 | Garnet–biotite schist | 575 ± 10[a] | Phase diagrams, Grt-Bt thermometry[a] |
| to13-7 | E103.680100 | N31.729210 | Garnet–biotite schist | 576 ± 10[a] | Phase diagrams, Grt-Bt thermometry[a] |
| to13-5 | E103.681183 | N31.725037 | Garnet–biotite schist | 508–583 ± 15 | Grt-Bt thermometry |
| lm09-220 | E103.710983 | N31.749128 | Garnet–biotite schist | n.a. | n.a. |
| lm147 | E103.722970 | N31.824930 | Biotite–white mica schists | 470 ± 15 | RSCM |
| lm09-52 | E103.728857 | N31.605644 | Metagranite in greenschist facies conditions | 370 ± 35 | Chl-Wm multi-equilibrium |
| lm09-53 | E103.730032 | N31.602583 | Metagranite in greenschist facies conditions | 370 ± 35 | Chl-Wm multi-equilibrium |
| to13-12 | E103.731531 | N31.599619 | Metadiorite in greenschist facies conditions | 370 ± 35 | Chl-Wm multi-equilibrium |

RSCM: Raman spectroscopy on carbonaceous material.

[a]Data from Airaghi, Lanari, et al. (2017).

JEOL JXA-8230 at ISTerre. Point analyses were acquired using 15 keV accelerating voltage and 12 nA beam current with a beam size between 1 and 3 μm. Representative mineral compositions are shown in Table 2. In order to track the chemical heterogeneity within the major minerals and allanite, X-ray maps of major minerals and allanite were acquired at 15 keV and 100 nA, a dwell time of 200 ms (300 ms for allanite) and were standardized using the program XMAPTOOLS 2.3.1 (Lanari, Vidal, et al., 2014). The mineral compositions of samples to13-4 and to13-7 are recorded in detail by Airaghi, Lanari, et al. (2017).

Garnet–biotite thermometry calculations were applied to sample to13-5 where garnet and biotite were observed in textural equilibrium, using the calibrations of Perchuk and Lavrent'eva (1983), Thompson (1976) and Holdaway and Lee (1977), at 10 kbar. The maximum temperature experienced by sample lm147 ($T_{peak}$) was estimated by Raman spectroscopy on carbonaceous material (RSCM) following the procedure described by Beyssac, Rouzaud, Goffé, Brunet, and Chopin (2002), as no garnet was observed in this sample. P–T conditions of the greenschist assemblage in the samples from the crystalline Tonghua massif were estimated with the multi-equilibrium chlorite–white mica–quartz–$H_2O$ thermobarometry, following the procedures described in Dubacq, Vidal, and De Andrade (2010), Lanari et al. (2012) and Airaghi, de Sigoyer, et al. (2017). Metamorphic conditions of the analysed samples are reported in Table 1.

## 3.2 | Metasedimentary rocks

Samples collected in the Silurian to Devonian metasedimentary series (to13-4, to13-5, to13-7, lm09-220 and lm147) are metapelites metamorphosed under amphibolite facies conditions, with assemblages of quartz+white mica+chlorite+garnet (except lm147) +biotite+ilmenite+ feldspar (albite) and accessory apatite+allanite (±monazite, Figures 2 and 3).

The relative chronological evolution of microstructures and mineral growth observed at the outcrop and thin section scales is summarized in Figure 2a. Samples to13-4, to13-7 (described in detail by Airaghi, Lanari, et al., 2017) and lm147 preserve an early white mica+chlorite-bearing S1 cleavage (related to the D1 phase of deformation). S1 is folded by a second S2 white mica-bearing crenulation cleavage associated with the D2 deformation (Figure 2b–d, g,h). In sample to13-5 and lm09-220, the S1 fabric is completely transposed into S2 (Figures 2e,f and 3b). Garnet grains appear as 400–600 μm (radius) porphyroblasts overprinting the S1 and S2 fabrics (e.g. Figure 2g). Biotite porphyroblasts of ~500 μm are either deformed by D2 (e.g. Figure 2b) or overprint the S1–S2 fabric (e.g. Figure 2d–f). Porphyroblasts were rotated during D3 (by different amounts depending on the sample) and incipient chlorite+white mica-bearing pressure shadows developed around biotite grains and at garnet rims (e.g. Figure 2d,g). At this stage, an S3 cleavage developed co-planar to S2, reactivating and folding the S2 fabric. Late euhedral grains of chlorite and white mica overprint all previous microstructures (especially in sample to13-5) and are oriented parallel to the microfold limbs associated with the S3-forming stage (e.g. Figure 2e; Airaghi, Lanari, et al., 2017).

In all the metapelites, allanite grains form 100–500 μm porphyroblasts subparallel to the S2 cleavage (Figure 3a), or cross-cut it (Figure 3b,c). No allanite grains were observed as inclusions in garnet. In samples to13-4 and to13-5, allanite has 10–15 μm thick Th-rich rims (Figure 3a,b) and exhibits small (a few μm in size) inclusions of quartz (~90%) and white mica (~10%, Figure 3a and Figure S1). In sample to13-
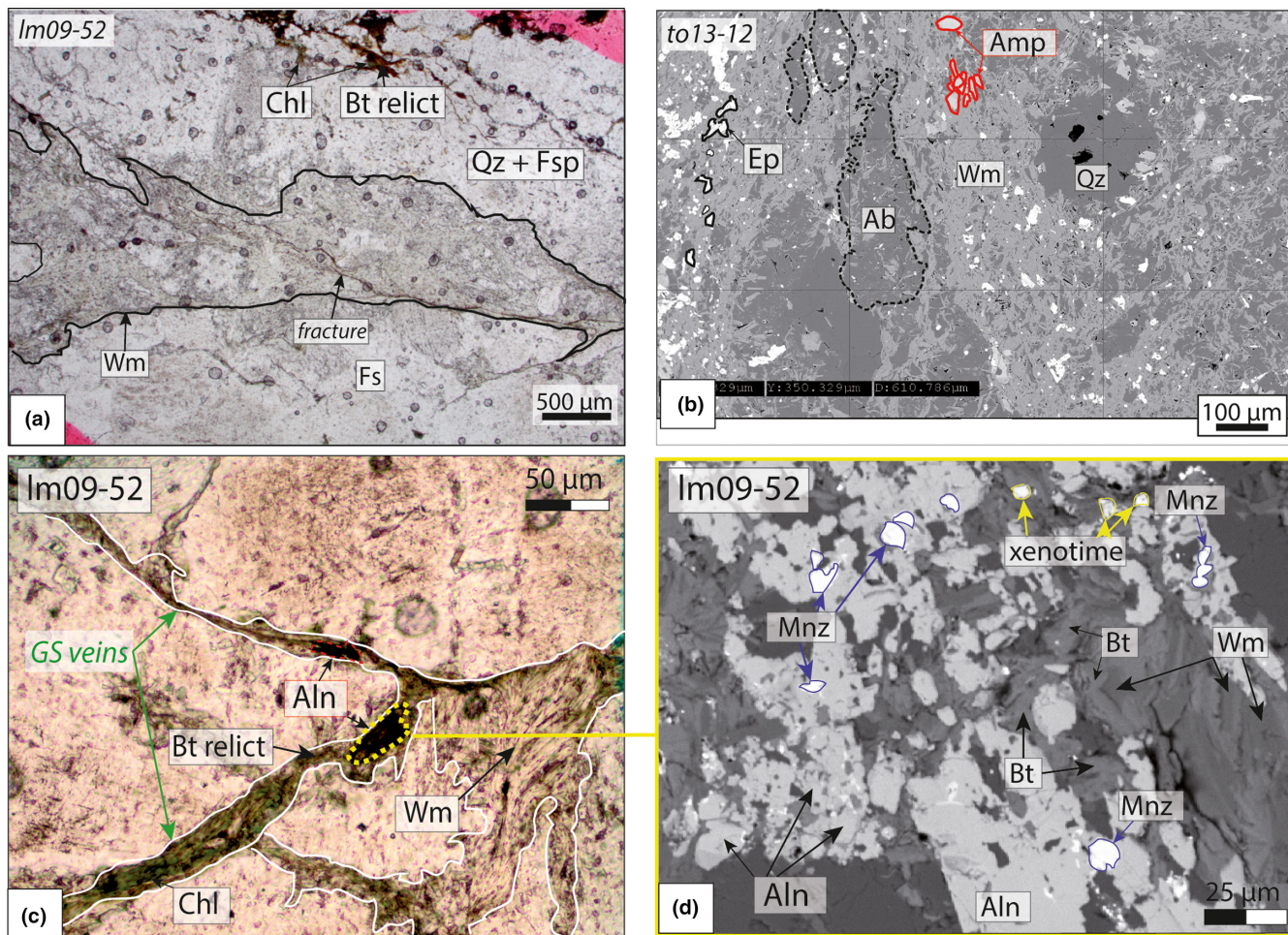
**FIGURE 4** Samples from the Tonghua crystalline massif. (a) PPL image of the white mica-bearing domains grown in deformed metagranite lm09-52. (b) BSE image of the white mica-bearing cleavage in deformed metagranodiorite to13-12. Red contours limit the amphibole grains. (c) PPL image of Chl+Wm+Aln-bearing greenschist veins (GS) in metagranite lm09-52. (d) BSE image of minerals associated with Aln in sample lm09-52

7, allanite is surrounded by monazite and epidote (Figure 3c). Qualitative compositional maps show chemical homogeneity in REE, U and Pb within the allanite grains (Figure S1).

The S1 and S2 fabrics are related to the prograde to peak metamorphic evolution (D1–D2 deformation stages in Figure 2a). Biotite and garnet are interpreted as index minerals that record the peak amphibolite facies conditions (Figure 2a; Airaghi, Lanari, et al., 2017; Worley & Wilson, 1996). In sample to13-5, biotite and garnet share sharp edges, suggesting that they grew in chemical equilibrium. Microtextures suggest that garnet and biotite are post-S2 (post-D2) or, as in sample to13-4, biotite growth was possibly syn- to post-D2. Due to its microtextural relationship with the S2 fabric, allanite is also linked to the peak metamorphic assemblage and is considered syn- to post-S2. The chlorite+white mica intergrowths at the biotite rims and the micrometric monazite at the allanite rims (in sample to13-7) appear related to the late metamorphic overprint under greenschist facies conditions, associated with the D3 deformation stage (Figure 2a).

The biotite porphyroblasts in samples to13-4 and to13-5 show an average $X_{Mg}$ of 0.43–0.46 (Table 2), with variations at the proximity of cleavage-parallel cracks that formed syn- or post- the S2-forming stage and towards the rims (increase in $X_{Mg}$ up to 0.51, Figure 5a). The Ti content in biotite porphyroblasts increases slightly from the core to the rims (0.08–0.14 pfu in to13-4, 0.07–0.09 for to13-4; Figure 5c).

Chemical heterogeneity is also observed in white mica. Compositional maps show that 10–15% of the white mica (muscovite is the major component) in the S2 cleavage in samples to13-4 and to13-7 has $Si^{4+}$ of 3.2–3.25 (Figure 5b) and $X_{Mg}$ of 0.54–0.61 (MsA following Airaghi, Lanari, et al., 2017). The remaining 80–85% of white mica, MsB, is found in the S2 cleavage, contains a lower $Si^{4+}$ of 3–3.15 and $X_{Mg}$ of 0.43–0.6 (Figure 5b). Heterogeneous chemical composition is also observed in matrix muscovite of sample lm147, where the $Si^{4+}$ varies from 3.1 to 3.3, for an $X_{Mg}$ of 0.65–0.72, and K varies from 0.84 to 0.91 (Figure 5d).

**TABLE 2** Representative chemical analyses for samples to13-5, lm09-52, lm09-53 and to13-12. Chemistry of samples to31-4 and to13-7 is described in detail by Airaghi, Lanari, et al. (2017)

| Sample Mineral | to13-4 Bt | to13-5 Bt | to13-5 Grt core | to13-5 Grt rim | lm147 Ms | lm09-53 Ms | lm09-53 Chl | lm09-52 Ms | lm09-52 Chl | to13-12 Ms |
|---|---|---|---|---|---|---|---|---|---|---|
| $SiO_2$ | 36.48 | 35.55 | 36.23 | 34.79 | 47.97 | 48.94 | 26.22 | 47.56 | 26.88 | 49.51 |
| $TiO_2$ | 1.33 | 1.48 | 0.05 | 0.04 | 0.399 | 0.63 | 0.06 | 1.57 | 0.04 | 0.08 |
| $Al_2O_3$ | 19.23 | 18.99 | 21.39 | 20.22 | 32.30 | 25.23 | 19.06 | 28.34 | 21.38 | 27.45 |
| FeO | 20.20 | 20.78 | 32.91 | 35.98 | 1.33 | 9.68 | 30.48 | 4.01 | 25.29 | 5.07 |
| MnO | 0.01 | 0.00 | 2.97 | 1.12 | 0 | 0.09 | 0.79 | 0.02 | 0.41 | 0.01 |
| MgO | 9.35 | 9.20 | 1.60 | 1.82 | 1.628 | 3.80 | 13.45 | 2.09 | 16.68 | 4.24 |
| CaO | 0.00 | 0.00 | 4.33 | 3.48 | 0.02 | 0.06 | 0.03 | 1.21 | 0.01 | 0.02 |
| $Na_2O$ | 0.27 | 0.22 | 0.02 | 0.05 | 0.37 | 0.10 | 0.05 | 0.20 | 0.02 | 0.12 |
| $K_2O$ | 8.28 | 7.61 | 0.01 | 0.05 | 10.07 | 10.25 | 0.07 | 10.28 | 0.04 | 8.72 |
| Total | 95.15 | 93.83 | 99.51 | 97.54 | 94.08 | 98.78 | 90.20 | 95.28 | 90.76 | 95.20 |
| Cations (pfu) | | | | | | | | | | |
| Si | 2.76 | 2.611 | 2.82 | 2.79 | 3.22 | 3.28 | 2.77 | 3.22 | 2.72 | 3.32 |
| Ti | 0.08 | 0.082 | 0.00 | 0.00 | 0.02 | 0.03 | 0.00 | 0.08 | 0.00 | 0.00 |
| Al | 1.72 | 1.645 | 1.96 | 1.91 | 2.55 | 1.99 | 2.37 | 2.27 | 2.55 | 2.17 |
| $Fe^{+2}$ | 1.28 | 1.277 | 2.14 | 2.41 | 0.07 | 0.54 | 2.69 | 0.23 | 2.14 | 0.28 |
| Mn | 0.00 | 0.000 | 0.20 | 0.08 | 0.00 | 0.01 | 0.07 | 0.00 | 0.04 | 0.00 |
| Mg | 1.05 | 1.007 | 0.19 | 0.22 | 0.16 | 0.38 | 2.12 | 0.21 | 2.52 | 0.42 |
| Ca | 0.00 | 0.000 | 0.36 | 0.30 | 0.00 | 0.00 | 0.00 | 0.09 | 0.00 | 0.00 |
| Na | 0.04 | 0.032 | 0.00 | 0.01 | 0.05 | 0.01 | 0.01 | 0.03 | 0.00 | 0.02 |
| K | 0.80 | 0.713 | 0.00 | 0.00 | 0.86 | 0.88 | 0.01 | 0.89 | 0.01 | 0.75 |
| Oxygen | 11 | 11 | 12 | 12 | 11 | 11 | 14 | 11 | 14 | 11 |
| $X_{Mg}$ | 0.45 | 0.44 | 0.08 | 0.08 | 0.69 | 0.41 | 0.44 | 0.48 | 0.54 | 0.60 |

## 3.3 | Crystalline basement

Samples lm09-52 and lm09-53 (from the Tonghua crystalline massif) are deformed metagranites; sample to13-12 is a deformed metagranodiorite (Figure 4). In all samples, the magmatic mineral assemblage of quartz+plagioclase+alkaline feldspar (+biotite in sample lm09-52) is overprinted by a greenschist mineral assemblage of albite+white mica+chlorite (+actinolite+epidote in sample to13-12). In samples lm09-52 and lm09-53, white mica and chlorite have grown in zones of localized strain, indicated by the subgrain rotation and grain size reduction of quartz. Both minerals also wrap feldspar and plagioclase grains and develop along micrometric-size fractures (Figure 4a). In sample to13-12, white mica grains form bands ~300 µm wide and are stretched along the main foliation. White mica-bearing layers alternate with albite-rich layers of few tens of micron wide (Figure 4b). In all samples, quartz exhibits undulatory extinction. Feldspar is strongly sericited and often shows perthitic "phantoms". Allanite was only found in sample lm09-52 (20–80 µm; Figure 4c). Grains are located in veins associated with titanite, apatite, biotite, xenotime (±monazite, ±zircon) and greenschist facies index minerals (chlorite and K-white mica; Figure 4c). Where allanite and titanite are in contact, the contact is irregular. Biotite generally shares sharp rims with titanite. Monazite and xenotime nucleated in rounded grains of 5–10 µm at allanite rims (Figure 4d).

Point analyses and compositional maps reveal that white mica (dominant muscovite composition of 60–65%) is chemically homogeneous within each sample (Table 2). In sample lm09-52, muscovite has a $Si^{4+}$ content of 3.18–3.22 pfu and $X_{Mg}$ of 0.44–0.54 (Figure 5e). Muscovite in sample lm09-53 contains $Si^{4+}$ of 3.2–3.3, but lower $X_{Mg}$ of 0.36–0.46. Finally, muscovite in sample to13-12 exhibits a higher $Si^{4+}$ of 3.2–3.5 and $X_{Mg}$ of 0.58–0.66. In samples lm09-52 and lm09-53, muscovite is associated with chlorite characterized by a $Si^{4+}$ of 2.7–2.8 (pfu) for an $X_{Mg}$ of 0.44–0.6. Microstructural observations suggest that titanite and biotite are of magmatic origin, overprinted by the allanite growth which preceded the metamorphic monazite+white mica+chlorite greenschist assemblage.
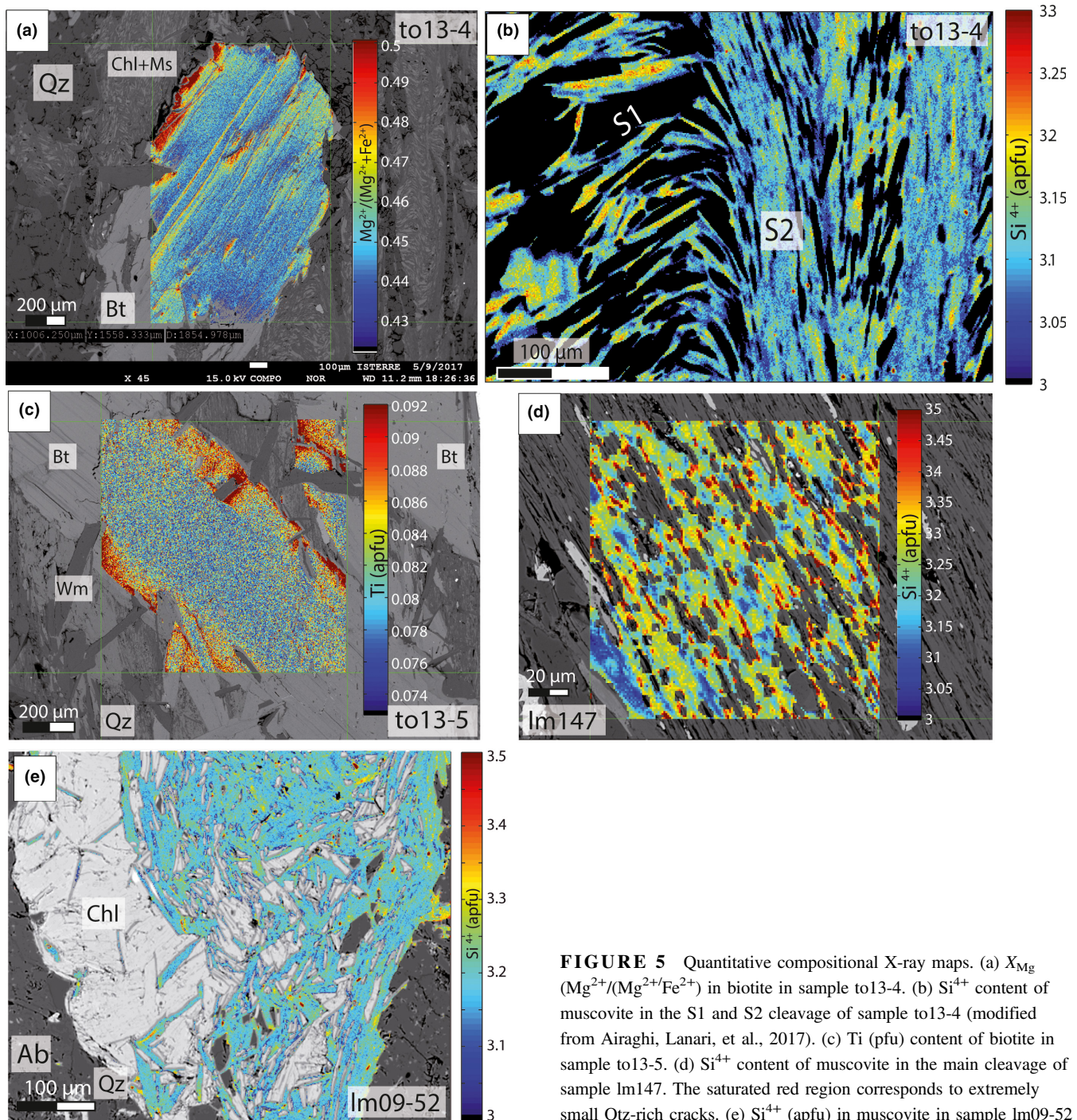
**FIGURE 5** Quantitative compositional X-ray maps. (a) $X_{Mg}$ ($Mg^{2+}/(Mg^{2+}/Fe^{2+})$) in biotite in sample to13-4. (b) $Si^{4+}$ content of muscovite in the S1 and S2 cleavage of sample to13-4 (modified from Airaghi, Lanari, et al., 2017). (c) Ti (pfu) content of biotite in sample to13-5. (d) $Si^{4+}$ content of muscovite in the main cleavage of sample lm147. The saturated red region corresponds to extremely small Qtz-rich cracks. (e) $Si^{4+}$ (apfu) in muscovite in sample lm09-52

## 3.4 | *P–T* framework

In metasedimentary rocks, temperatures obtained from garnet–biotite thermometry for sample to13-5 range between 508 and 583 ± 15°C (Table 1). The temperatures from biotite–garnet core analysis pairs range between 508 ± 15 and 541 ± 15°C, which are systematically lower than rim analysis pairs which range between 523 ± 15 and 583 ± 15°C. Sample lm147, located far from the WF and

in an upper structural level of the sedimentary series, yields an RSCM $T_{peak}$ of 470 ± 15°C (Table 1).

In samples from the crystalline massif, multi-equilibrium thermobarometry constrains the greenschist facies *P–T* conditions to 7 ± 1 kbar, 370 ± 35°C (see Figure S2). No chlorite was observed in sample to13-12; it was therefore not possible to directly calculate the pressure of muscovite growth. Results show that the greenschist overprint in the Tonghua crystalline massifs occurred at lower conditions

than in its metasedimentary cover (<405°C), but at higher pressure conditions (>6 kbar).

Our new thermometric estimates for these metasedimentary rocks are consistent with those of Airaghi, Lanari, et al. (2017) that relate the composition of MsA in samples to13-4 and to13-7 to peak pressure conditions (11 ± 2 kbar, 530 ± 20°C) and the composition of MsB to peak temperature conditions (6.5 ± 1 kbar, 575 ± 10°C). The garnet–biotite-bearing assemblages observed in sample to13-5 and lm09-220 suggest that they experienced peak metamorphic conditions similar to samples to13-4 and to13-7. Muscovite grains located in biotite pressure shadows and at biotite rims (MsC) in samples to13-4 and to13-7 are related to the greenschist facies overprint at 4 ± 1 kbar, 380–450°C (Airaghi, Lanari, et al., 2017). Muscovite replacement therefore took place at the peak-*P*, peak-*T* and during the greenschist overprint by pseudomorphic replacement and dissolution–reprecipitation (Airaghi, Lanari, et al., 2017 and references therein).

## 4 | U–Pb/Th GEOCHRONOLOGY

### 4.1 | Methods

LA-ICP-MS U–Th/Pb dating of allanite was performed in situ on the same polished thin sections used for the microstructural, petrological and thermobarometric studies (Airaghi, Lanari, et al., 2017; this study). Allanite was analysed at the Institute of Geological Sciences, University of Bern using a GeoLas Pro 193 nm ArF excimer laser ablation system coupled with an ELAN DRC-e quadrupole ICP-MS (full details are provided in Appendix S1). Isotope ratios were evaluated using the Th-isochron approach because the variability in U meant that the Terra–Wasserburg regression (Tera & Wasserburg, 1972) did not allow a regression line to be calculated precisely (e.g. Janots & Rubatto, 2014; Appendix S1). During the integration process, analyses exhibiting any age zoning were discarded. Therefore, any potential effect of inclusions was identified and eliminated. The U–Pb and Th values obtained for allanite within each sample were processed as a single population and used to calculate a single weighted mean age. This was in agreement with our petrological observations, which suggested only a single allanite growth stage within each sample.

### 4.2 | Results

Around 15 analyses were collected from each sample. Four grains of allanite were analysed in metapelite to13-4 and metagranite lm09-52, seven in metasedimentary sample to13-7 and three in metasedimentary sample to13-5. All analysed allanite contains higher Th than U and highly variable initial Pb concentrations (Table S1). Within

individual samples, the U–Pb dates were concordant with Th–Pb dates, but were more dispersed and more significantly affected by small variations in common Pb concentration (see Figure 6a,b for a comparison). We therefore used the Th–Pb dates for age interpretations.

Allanite in metapelites to13-4 and to13-5 yielded Th–Pb ages of 191.0 ± 9.6 Ma and 191.0 ± 22.0 Ma respectively (Figure 6a,c). Sample lm09-220 yielded ages of 180.4 ± 6.4 Ma (Figure 6d). Allanite in sample to13-7 yielded ages of 201.0 ± 22.0 Ma (Figure 6e). Finally, allanite in sample lm09-52 (Tonghua crystalline massif) yielded ages of 176.0 ± 22.0 Ma, within the error of the metasedimentary cover ages (Figure 6f).

## 5 | $^{40}Ar/^{39}Ar$ CHRONOLOGY

### 5.1 | Methods

Metapelites to13-4, to13-5 and lm147 and Tonghua crystalline massif samples to13-12 and lm09-52 were selected for in situ $^{40}Ar/^{39}Ar$ mica dating. Samples were dated at The Open University, UK, following the procedure detailed in Appendix S1. One sample, to13-12, was analysed at the University of Montpellier, France following the procedure described in Airaghi, de Sigoyer, et al. (2017). All Montpellier dates were recalculated using the decay constant and standard ages used for calculating dates at The Open University (Appendix S1). Biotite and muscovite were analysed in polished 300 μm thick sections to link ages to microstructural position. Both in situ infrared (IR) laser (melting) and in situ ultraviolet (UV) laser (ablation) methods were used (Figure 7a–d; see below). Data are reported in Table S2. Age uncertainties are reported to 2σ; uncertainties on the isotopic measurements are reported to 1σ.

### 5.2 | Results

The $^{40}Ar/^{39}Ar$ analyses are reported in Figures 7 and 8 and in Table S2. Biotite in sample to13-5 yielded UV laser $^{40}Ar/^{39}Ar$ dates ranging from 230 ± 17 to 201 ± 7 Ma (the date with the largest uncertainty being at 233 ± 58 Ma) for grain cores and from 183 ± 12 to 159 ± 10 Ma for grain rims (the majority of the analyses ranging between 183 ± 12 and 176 ± 13 Ma, Figure 7a, b). Ages yielded by IR laser analyses range from 189.7 ± 1.2 Ma (mean biotite core) to 171.1 ± 1.4 Ma (mean biotite rim; white and black squares in Figure 7d). In sample to13-4, it was more difficult to spatially resolve the core and the rim ages of biotite, given the lower resolution of the IR laser technique (Figure 7c). For this sample, ages range from 215.5 ± 3.3 Ma to 187.6 ± 0.9 Ma (green circles in Figure 7d).
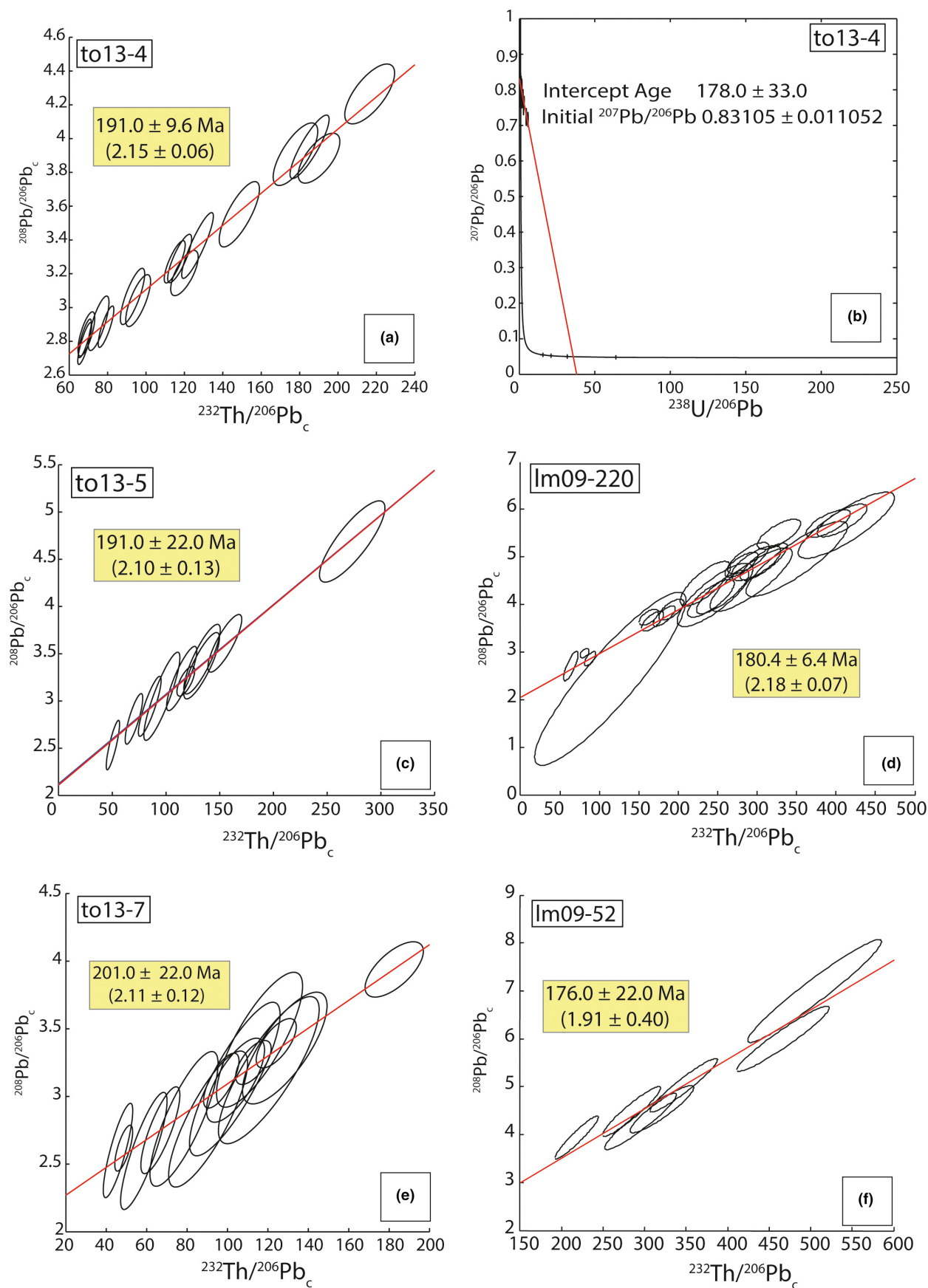
**FIGURE 6** Th–Pb allanite ages (a, c, d, e and f). Each ellipse represents one analysis. Initial values of common $^{208}Pb/^{206}Pb_c$ are indicated in brackets below the age in the yellow frames. Panel (b) is an example of Tera–Wasserburg diagram for sample to13-4

Muscovite of generation MsA was not successfully dated since grains were too small and intergrown with chlorite, the analysis of which contaminated the Ar signal. The majority of the white mica grains stretched along the main S2 cleavage (MsB in Figure 8a) in metapelite to13-4 yielded in situ laser ablation ages ranging from $168 \pm 9$ to $136 \pm 7$ Ma with four older ages ranging from $210 \pm 22$ to $173 \pm 13$ Ma (blue circles in Figure 8b). The spatial resolution of the ablation spot was not sufficient to distinguish between different core and rim ages. Three ages ranging between $130 \pm 0.7$ and $128 \pm 0.8$ Ma were yielded by IR laser melting in the same sample (see Table S2). The $^{40}Ar/^{39}Ar$ muscovite dates obtained in the S2 cleavage of sample lm147 (Figure 8c) range from $159 \pm 3$ to $150 \pm 1$ Ma (grey in Figure 8b). In the crystalline basement, muscovite domains of samples lm09-52 and to13-12 (Figure 8d) yielded $^{40}Ar/^{39}Ar$ dates ranging from $141 \pm 7$ to $122 \pm 4$ Ma and from $131 \pm 17$ to $122 \pm 4$ Ma respectively (red and blue in Figure 8b).

# 6 | P–T–t INTERPRETATION

## 6.1 | Analytical uncertainty of the geochronological data

The Th–Pb ages obtained for allanite in the metasedimentary cover at different locations range between c. 223 and 169 Ma (Late Triassic–Early Jurassic), but dates yielded by individual samples all overlap within error. U–Pb ages were concordant with Th–Pb ages for all analysed samples. The age uncertainty mainly results from relatively high quantities of common Pb incorporated in the allanite grains. All allanite analyses exhibit a $^{208}Pb/^{206}Pb$ ratio close to the 200 Ma reference value of 2.09 obtained from the "global lead evolution model" of Stacey and Kramers (1975). The metasedimentary cover seems therefore to have experienced a consistent metamorphic history at the Late Triassic–Early Jurassic.

The core to rim variation in age uncertainty in biotite of sample to13-5 is independent of the intensity of the $^{40}Ar$ signal and different ages do not significantly overlap within the error. This is also the case for ages obtained for the same sample with the IR technique. Despite the chemical heterogeneities of the mica grains, the in situ IR approach provides an independent check on the age measured with the UV in situ approach.

The similarity between results obtained with the two extraction methods suggests that both extraction techniques sample the same age population(s). However, in the IR results, some of the "bt core" dates plot close to the "bt rim" dates. This may be due to the lower spatial control, resulting in a potential mixing of Ar released from different age zones during laser melting. In sample

to13-4, the spatial control of the IR laser ablation was lower than in sample to13-5 and the zoning more patchy (see Figure 5a), resulting in indistinguishable ages between the core and the rims of biotite (green in Figure 7d). In this case, all single biotite dates overlap within error. The probability distribution function (PDF) obtained for all biotite analyses clearly show two peaks at c. 220–210 and c. 180 Ma (Figure 7e), supporting the existence of two age populations.

In sample to13-4, no significant correlation is observed between the intensity of the $^{40}Ar$ signal and the dates, although the dates with the lowest uncertainties correspond to the ones with a $^{40}Ar$ signal >0.04 V (Figure 8b; Table S2). Older ages do not overlap within error with muscovite ages clustering at c. 140 Ma. Data were also plotted in a $^{36}Ar/^{40}Ar$ v. $^{39}Ar/^{40}Ar$ and $^{40}Ar/^{39}Ar$ v. $^{38}Ar/^{39}Ar$ diagrams to potentially distinguish among different generations, but the plots were uninformative (full data are available in Table S2). In sample lm147, the ages of different grain sizes and associated chemical heterogeneities were too small to be differentiated with the spatial resolution of the laser, but their ages are consistent with the youngest muscovite ages in sample to13-4.

In the Tonghua crystalline massif, allanite grains from sample lm09-52 yield ages of 198–154 Ma, within the uncertainty of the time interval yielded by both muscovite and allanite in the metasedimentary cover. Muscovite in the crystalline massif only preserves the youngest event (at c. 130 Ma) recorded in the sedimentary cover. The PDF of all muscovite dates (Figure 8e) shows that the majority of dates lie between 150 and 120 Ma (with the youngest contribution derived from analyses in the crystalline basement). There are also older contributions at c. 170 Ma and between 220 and 180 Ma.

## 6.2 | P–T–t path implications

The integration of new and previously acquired thermobarometric data with geochronological results provides major insights into the P–T–t path followed by the rocks of both the internal sedimentary cover and the basement in the central Longmen Shan (Figure 9a,b). The chemical homogeneity of allanite and its microstructural location aligned along the S2 cleavage, exhibiting S2-parallel inclusions (as in sample to13-4) or overprinting the S1–S2 (as in sample to13-5, see Section 3.2), suggest that it grew during a single event either during or after the S2 fabric-forming stage (syn- to post-D2). Allanite growth may correlate with fluid pulses occurring along the prograde to peak path (Airaghi, Lanari, et al., 2017), thus marking the attainment of pressure-peak or temperature-peak conditions (Figure 9a). However, no allanite was observed included in
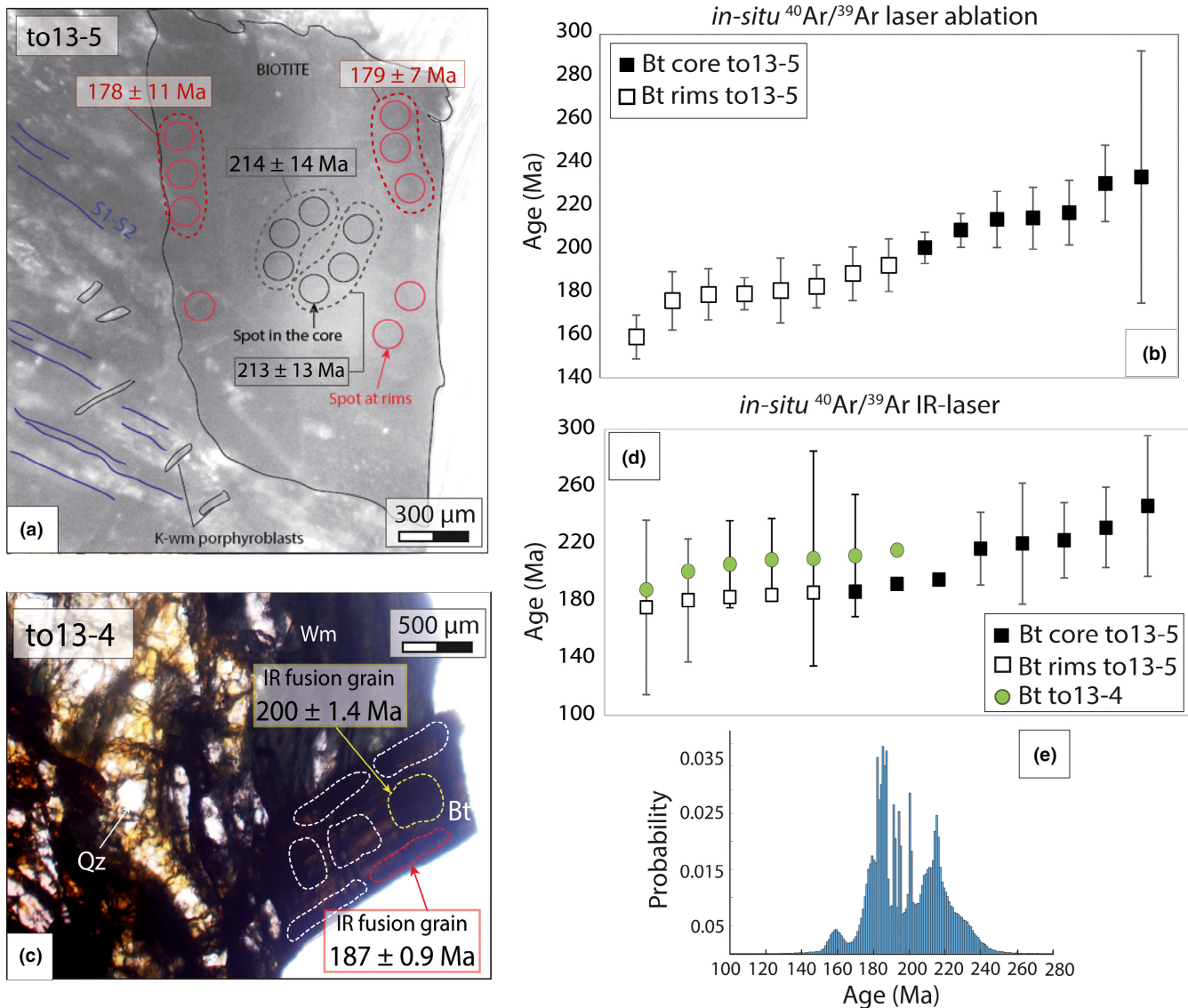
**FIGURE 7** $^{40}$Ar/$^{39}$Ar results for biotite in samples to13-5 and to13-4. (a) Reflected light image of a biotite grain in sample to13-5. Representative locations of laser spots are indicated by circles. (b) $^{40}$Ar/$^{39}$Ar ages for biotite core (black) and rims (white) obtained with the in situ UV ablation technique for sample to13-5. Analyses are shown plotted from young to old. (c) Reflected light image of analysed biotite grains in sample to13-4. (d) IR laser $^{40}$Ar/$^{39}$Ar ages for biotite core (black) and rims (white) for sample to13-5 and to13-4 (green circles) obtained with the in situ IR single grain fusion technique. (e) Probability distribution function (PDF) of all biotite ages obtained for 10,000 random iterations (Monte Carlo approach) generated from the age and uncertainties measured values

garnet, suggesting that its growth post-dates that of garnet (peak-*P*, Airaghi, Lanari, et al., 2017), and is closer to the peak-*T* (Figure 9b). The allanite ages in sample lm09-220 show the smallest uncertainties and are likely to provide the best estimate for the timing of the peak-*T* (at 180 ± 6.4 Ma), assuming that allanite grew in the same time interval in different studied samples as suggested by microstructures.

Previous microstructural observations and thermobarometric estimates suggest that biotite started to grow prior to (or along with) garnet during the prograde path, but

experienced a pulse of growth at the peak-*T*, where the majority of the large porphyroblasts developed (samples to13-4 and to13-7; Airaghi, Lanari, et al., 2017; Figure 9a, b). The large interval of biotite growth is also supported by the fact that biotite is both deformed by D2 (to13-4) or overprints the S2 cleavage. The chemical heterogeneity of biotite may also be suggestive of long-lasting growth. Biotite $^{40}$Ar/$^{39}$Ar ages obtained with both the in situ laser ablation and IR laser techniques for sample to13-5 are in good agreement with IR laser biotite ages of sample to13-4 (Figure 7d). Biotite in both samples thus records the same
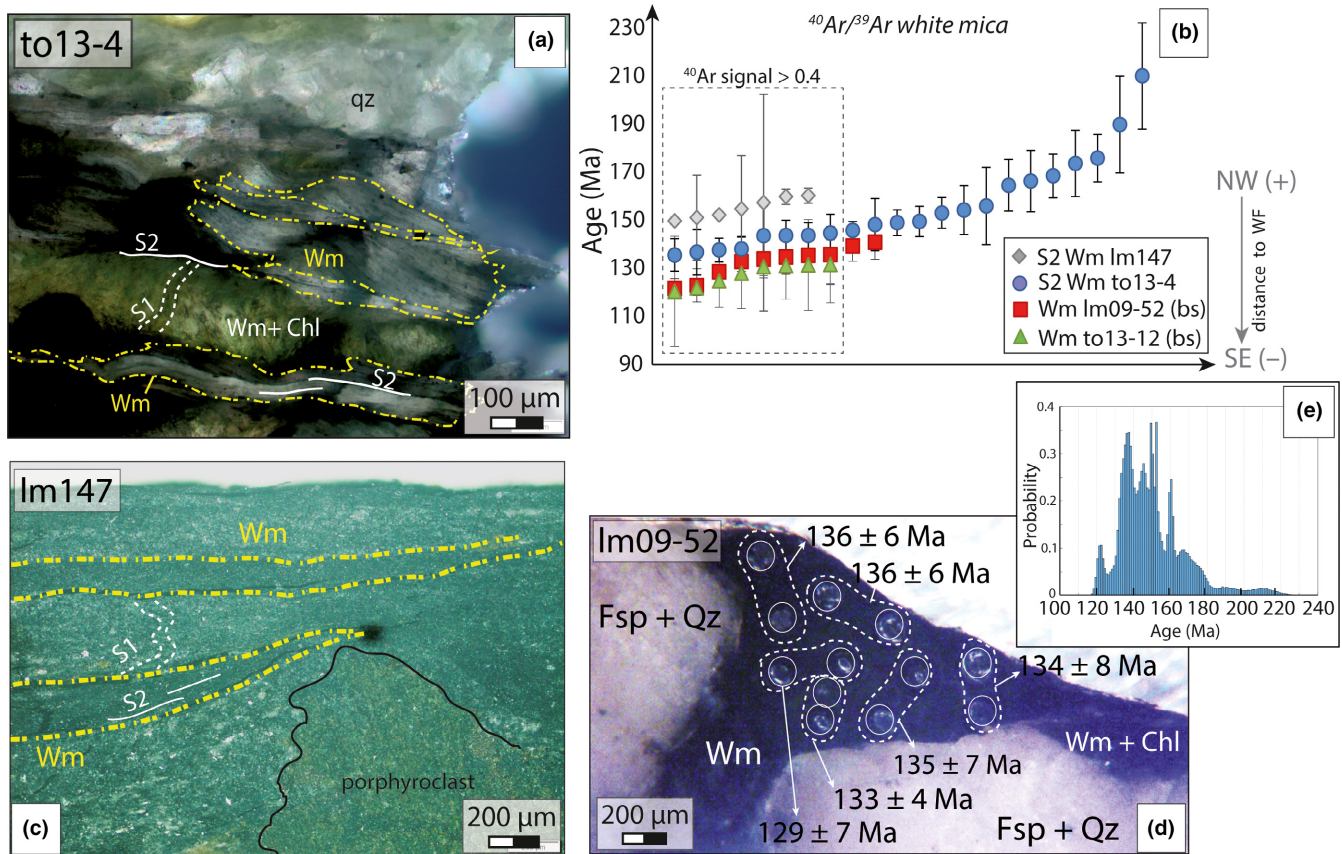
**FIGURE 8** $^{40}$Ar/$^{39}$Ar results for white mica (Wm) in samples to13-4, lm147, lm09-52 and to13-12. Dashed yellow lines limit the domains dated by $^{40}$Ar/$^{39}$Ar. (a) Analysed S2-forming Wm (yellow) in sample to13-4. (b) In situ UV (to13-4, lm09-52 and to13-12) and IR (lm147) $^{40}$Ar/$^{39}$Ar ages for all analysed Wm with relative errors. Analyses are shown plotted from young to old. WF = Wenchuan fault. (c) Analysed muscovite in sample lm147. (d) Analysed Wm domains in metagranite lm09-52. Laser spots are indicated by circles. One analysis (white dashed line) includes two spots. (e) Probability distribution function for all Wm ages (generated as in Figure 7)

metamorphic event. Furthermore, their ages also overlap the allanite ages. Despite peak temperatures >550°C (well above the closure temperature for Ar in biotite at ~280°C, for a 100 μm biotite grain cooling at a rate of 1°C/Ma, Harrison, Duncan, & McDougall, 1985), $^{40}$Ar/$^{39}$Ar ages in biotite grains seem therefore to have recorded the timing of their crystallization and to not have undergone significant loss of Ar by diffusion. The ability of biotite to retain Ar at >500°C has already been documented by Villa (2015) and might be extended here up to 580°C. Biotite in amphibolite facies rocks in the Himalayas also commonly records ages consistent with the timing of prograde growth (e.g. Stübner et al., 2017), although the older ages are commonly interpreted as being due to the presence of excess $^{40}$Ar. The Ar inherited from the first biotite that grew during the prograde to peak metamorphic path in our samples may have contributed to the old ages. We cannot, however, exclude that biotite porphyroblasts might also have retained a part of the Ar signature of the early muscovite (MsA) from which it partially developed—this has implications

for the current understanding of Ar closure temperatures in biotite.

Muscovite in the S2 cleavage of samples to13-4 and to13-7 (MsB in Figure 9a,b) chemically re-equilibrated at the peak-$T$ (Airaghi, Lanari, et al., 2017), but preserves older cores formed at peak-$P$ conditions (MsA in Figure 9a,b; Section 3.2). The fact that relics of the MsA generation were smaller than the Ar laser spot may explain the variety of ages obtained for MsB. In particular, a partial sampling of the MsA may explain the spread of ages between 210 and 156 Ma (Figure 8e), the upper limit being similar to the ages recorded in the biotite core. Previous studies have shown that white mica grains (or parts of grains) that escaped chemical re-equilibration can also avoid Ar loss (Hames & Cheney, 1997).

However, the majority of the in situ UV $^{40}$Ar/$^{39}$Ar muscovite data from multiple samples and the ones with the lowest uncertainties in sample to13-4 yield much younger ages between 150 and 124 Ma (Figure 8b,e), younger than the ages yielded by biotite. Detailed petrological analysis
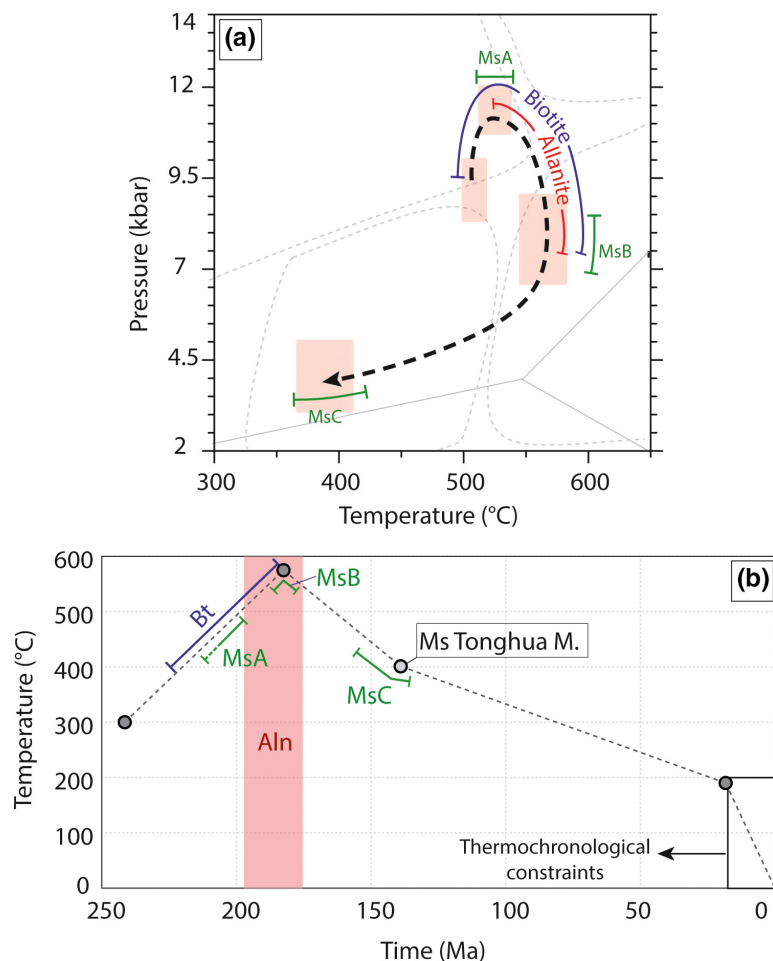
**FIGURE 9** Estimated *P–T–t* path for the internal metasedimentary units from petrological and geochronological constraints (see text for details). Tonghua M = Tonghua crystalline massif. The age of MsA is not directly measured but deduced from *P–T* relations and allanite ages (see text). The rapid *T–t* variation in the last 10 Ma in panel (b) is constrained by apatite and zircon fission track thermochronology and (U–Th–He) data collected in the crystalline massifs (Kirby et al., 2002; Wang et al., 2012; Tan et al., 2017 and references therein and in the text). Time is from 250 Ma to present (left to right)

of two areas of samples to13-4 and to13-7 reveals little late MsC in the S2 cleavage (<0.5%), but rather only in porphyroblast pressure shadows. This might, however, not be representative of the all dated areas, where the percentage of the MsC within the S2 might be variable.

In the samples from the Tonghua crystalline massif, the scarce preservation of the allanite-bearing assemblage makes it difficult to precisely assess the metamorphic conditions of allanite growth. However, there is no evidence of metamorphic conditions higher than the greenschist facies (7 ± 1 kbar, 370 ± 35°C, sample lm09-52). The Th–Pb allanite ages (sample lm09-52) constrain the timing of allanite growth at 176.0 ± 22.0 Ma. Muscovite records younger ages than allanite, in agreement with textural relationships (see Section 3.2). In samples lm09-52 and to13-12, the $^{40}Ar/^{39}Ar$ dates obtained for muscovite in two different Ar laboratories are consistent at *c.* 140–130 Ma, supporting the precision of the data and discarding the hypothesis of a constant mixing age. The existence of a single chemical population of muscovite also suggests that the mixing of different populations is unlikely. The estimated conditions for the greenschist metamorphism are consistent with the *P–T* conditions estimated for the growth of late muscovite and chlorite grains in the metasedimentary

cover (MsC in Figure 9a) (Airaghi, Lanari, et al., 2017). The temperature estimated for the greenschist facies overprint (≤400°C) is in this case below the nominal closure temperature of Ar in muscovite (425°C for 100 μm radius grain and a cooling rate of 10°C/Ma, Harrison, Célérier, Aikman, Hermann, & Hizler, 2009) but close to its lower limit (405°C, for the same conditions). We therefore relate $^{40}Ar/^{39}Ar$ dates to the crystallization of white mica between 140 and 120 Ma with some scatter due to $^{40}Ar$ contamination; low $^{40}Ar$ signal for some analyses (responsible for the ages with the largest uncertainties); and $^{40}Ar$ loss due to resetting, fluids or diffusion (responsible for the youngest ages). The greenschist facies metamorphic event thus affected the Tonghua crystalline massif at 140–120 Ma.

Overall, the regional consistency of the $^{40}Ar/^{39}Ar$ ages between 150 and 124 Ma (Figure 8e) corroborates the geological significance of the Early Cretaceous muscovite ages and discards the hypothesis of the presence of a significant amount of excess $^{40}Ar$ into the analysed minerals. We would expect $^{40}Ar$ contamination to vary on both the sample and grain scale.

The integration of the petrological and geochronological results for the metasedimentary cover shows one major result: biotite seems to be able to retain crystallization ages

at relatively high temperatures, while the majority of the muscovite in the S2 cleavage does not. This difference might be (1) an effect of a protracted and slow cooling history, driving differences in Ar diffusion rates in muscovite and biotite characterized by a different grain size. At the temperatures experienced by the studied rocks, diffusion is generally considered to be one of main processes affecting Ar concentration in the mica grain. Alternatively, the difference in biotite and muscovite ages may (2) indicate different Ar crystallization and re-equilibration histories through the different metamorphic stages (D1, D2 and D3). In order to discriminate between hypotheses (1) and (2), we tested different thermal scenarios in a series of simple Ar diffusion modelling experiments.

# 7 | DIFFUSION MODELLING

Two sets of cooling paths were tested (Figure 10): (1) simple cooling paths from 186 Ma (the reference age of the thermal peak) and (2) more complex cooling paths constrained by independent geochronological and thermochronological data (see Section 1; Godard et al., 2009; Kirby et al., 2002; Tan et al., 2017 and references therein). The MATLAB™-based program DiffArg (Wheeler, 1996; modified by Warren, Hanke, et al., 2012; Warren, Sherlock, & Kelley, 2011; C. J. Warren, pers. comm.) was used to determine whether there was a simple cooling scenario that best fitted the data. All model experiments were run for scenarios where temperature was decreased from a $T_{peak}$ of 580°C at 186 Ma (Airaghi, Lanari, et al., 2017; this study), for a biotite grain radius of 0.5 mm and a muscovite grain radius of 0.05 mm (similar to that observed in thin section). In the model, the MsB grains were considered homogeneous (without the MsA inheritance) to predict the age of only the grains that completely re-equilibrated at the peak-$T$ at $c$. 186 Ma, and check if it could approach the interval of 150–124 Ma. The pressure was assumed constant at 10 kbar as a first-order approximation. The role of fluid in Ar mobility is not considered in the model: it purely solves for thermally activated diffusion.

The prograde path (from 530 to 580°C, from 230 to 185 Ma; Figure 9b) was not modelled since at these temperatures, it has already been shown by Ar diffusion models that no Ar is retained over geologically meaningful time-scales in an open system (Warren et al., 2011). The Ar diffusion model was therefore only run for the 186 Ma time period *after* the peak-$T$.

Following previous studies, the Crank–Nicholson solver was used, with a time integration step of 10 (Wheeler, 1996). A cylindrical diffusion geometry was assumed for both mica phases (Hames & Browring, 1994), but with different diffusion lengths for muscovite and biotite (Wheeler,

1996 and references therein). The numerically converged bulk age was calculated following the method outlined in Warren, Hanke, et al. (2012).

We tested a series of models with simple cooling paths, with temperature decreasing linearly at rates of 2, 15 and 30°C/Ma respectively (P1, P2 and P3 in Table 3 and Figure 10a) to understand the behaviour of the Ar record for different thermal histories. Following other thermochronology constraints from the literature—mainly obtained for the crystalline massifs and covering the last 30 Ma—we also explored two more complex synthetic temperature paths (paths A and B in Table 3 and Figure 10b) where temperature decreases linearly between the different $T$–$t$ segments. In path A, temperature decreases from 580 to 400°C at 4°C/Ma (constrained by this study's results for the Tonghua massif) and from 400 to 0°C at 2.8°C/Ma such that 0°C is reached after 186 Ma model time (constant cooling as suggested by Roger et al., 2011). In path B, temperature decreases from 580 to 400°C at 4°C/Ma as above, then from 400 to 200°C at 1.5°C/Ma (based on the fission track and U–Th/He ages of Godard et al., 2009; Kirby et al., 2002; Tan et al., 2017) and subsequently cools to reach 0°C after 186 Ma model time (Table 3).

The best-fit model solutions were initially investigated for biotite, with the resulting model then tested on muscovite. All models were run for open system scenarios. Core and rim ages (50–100 μm from the rim in the analysed samples) were used to test the fit of the model rim age predictions. Model uncertainties are described in detail in Mottram, Warren, Halton, Kelley, and Harris (2015). In summary, the experimentally derived diffusion parameters provide the greatest source of uncertainty, and in these models would shift the resulting bulk age ±4 Ma.

The predicted model ages for biotite that cooled from 580 to 0°C at 2, 15 and 30°C/Ma (models P1, P2 and P3) are 58, 171 and 177 Ma respectively (Figure 10a). The bulk ages predicted for biotite cooling along path A are 131 Ma, whereas those for path B are 110 Ma. Muscovite models predicted ages of 93, 175 and 181 Ma for P1, P2 and P3 respectively (Figure 10a), and 140 and 133 Ma for open system paths A and B respectively (Figure 10b).

# 8 | DISCUSSION

## 8.1 | Different Ar histories for biotite and muscovite

In all model experiments, regardless of the rate at which the system cooled, predicted biotite ages were significantly younger than the measured ones, as expected when following the closure temperature formulation. Constant cooling rates higher than 30°C/Ma (P3) are unlikely for the area, since they would imply that metasedimentary units reached
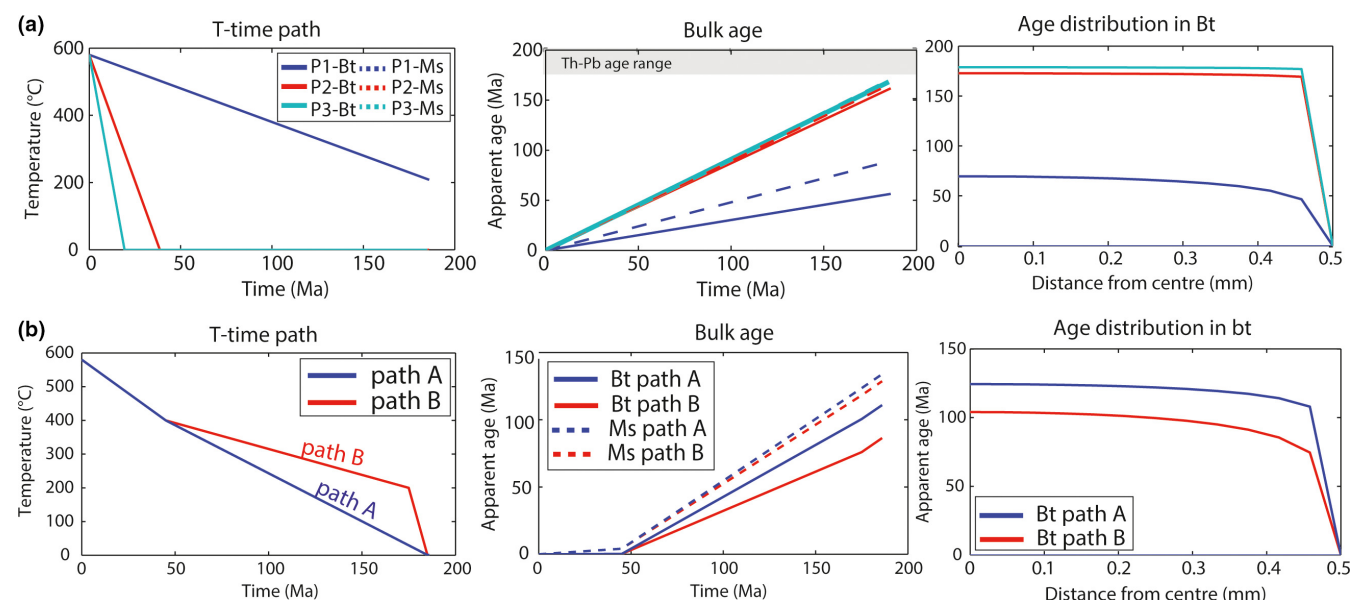
**FIGURE 10** Results of Ar diffusion modelling experiment for biotite (radius 0.5 mm) and muscovite grains (radius 0.05 mm) for cooling paths P1, P2 and P3 in an open system (a), and for path A and B in an open system (b). Time is "model time," which means that 0 = time of the temperature peak and 186 Ma = present day. The left diagrams are the modelled temperature paths; middle diagrams represents the variation of the age integrated over the grain distance (bulk age) with time; right diagrams are the core to rim age variation within a single biotite grain. Grey box: range of Th–Pb allanite ages

**TABLE 3** $T$–$t$ paths tested in Ar diffusion modelling experiments. Model time is the time passed from the $T$-peak stage, where $t = 186$ Ma is the present day

| Path | $T_{peak}$ (°C) | Model time (Ma) | $T$ (°C) | $T$ decrease |
|------|------|------|------|------|
| P1 | 580 | 186 | 208 | Linear |
| P2 | 580 | 39 | 0 | Linear |
| P3 | 580 | 19.9 | 0 | Linear |
| A | 580 | 45 | 400 | Linear |
|   |   | 186 | 0 | Linear |
| B | 580 | 45 | 400 | Linear |
|   |   | 175 | 200 | Linear |
|   |   | 186 | 0 | Linear |

the surface by 165 Ma, in contrast with previously published thermochronological data. It was instead possible to approach the measured age on muscovite at 150–124 Ma with model experiments performed along the $T$–$t$ paths A and B. However, the fact that the mica ages are uniform among different samples (and over 200 km) suggests that these highly contrived open system models should be invoked for all samples experiencing relatively high temperatures (>500°C), and therefore also for biotite. Nevertheless, these models are completely unable to account for the difference between biotite and muscovite ages. This suggests that the age differences between biotite and mica cannot be ascribed to diffusion due to slow cooling in minerals with different grain sizes and strengthens the

hypothesis that biotite and muscovite experienced different growth and resetting histories that affected Ar concentration in different ways, as strongly suggested by petrological observations. In particular, the age difference may indicate that (1) the system remained open to Ar for muscovite in the S2 cleavage longer than for biotite porphyroblasts, until the temperature–deformation–fluid conditions were not able to promote Ar resetting and/or that (2) muscovite in the S2 cleavage experienced a post peak-$T$ crystallization event (marked by the growth of MsC) that biotite did not experience, leading to the partial resetting of the Ar system.

## 8.2 | Role of microstructural position and replacement reactions on $^{40}$Ar/$^{39}$Ar ages

From a petrological and microstructural point of view, the age difference between biotite and muscovite for the $^{40}$Ar/$^{39}$Ar system might have been favoured by different factors:

1. *Different microtextural sites for biotite and muscovite.* Several studies have shown that deformation can act as a network for inter-grain loss of radiogenic $^{40}$Ar (Cossette, Schneider, Warren, & Grasemann, 2015; Kramar, Cosca, & Hunziker, 2001; Mulch, Cosca, & Handy, 2002). The elongated muscovite forming the main S2 cleavage was likely to have preferentially accommodated the post peak-$T$ deformation over the large

porphyroblasts of biotite, preventing extensive $^{40}$Ar re-equilibration in biotite.

2. *Fluid-driven replacement of MsB by MsC.* Petrological analyses show a compositional variability in muscovite of these samples (see Section 3 and Figure 5). Although MsC is not the major constituent of the S2 cleavage in the thin section areas that we studied in detail, its percentage might vary within the sample and within the analysed areas. Furthermore, the laser spot size used during the $^{40}$Ar/$^{39}$Ar analyses was, on average, larger than the spatial scale of the muscovite chemical heterogeneity. The ages of muscovite in the S2 cleavage might therefore represent a mixture between two end-members with the oldest ages approaching the age of growth of MsA and the youngest ages approaching the crystallization ages of MsC. It has been documented that white mica can preserve crystallization ages at least up to 500°C, depending on the length of time the rock experienced those temperatures and the openness of the grain boundary system (Villa, 2015; Warren, Hanke, et al., 2012). The occurrence of a recrystallization (or muscovite replacement) event at 150–124 Ma instead of simple cooling is also supported by the fact that the sample in an upper structural position (lm147) seems to record only the youngest event and that the muscovite generation observed in the Tonghua crystalline massif grew in the same time interval.

3. *Acquired intra-grain porosity in muscovite.* Petrological results show that while MsB partially re-equilibrated at the peak-*T* (except relicts of MsA peak muscovite), biotite porphyroblasts never experienced recrystallization after their growth at the peak-*T*. While muscovite recrystallization during metamorphism is a more efficient mechanism for Ar resetting than diffusion (Allaz et al., 2011; McDonald et al., 2016; Villa, 1998), the absence of recrystallization in biotite may instead preserve crystallization ages (Di Vincenzo et al., 2001; Kelley, 1988; Villa, 2016). The intra-grain porosity of newly crystallized biotite grains is likely to be lower than the intra-grain porosity of muscovite grains partially replaced during the *P–T* path by "pseudomorphic replacement" (Airaghi, Lanari, et al., 2017; Putnis, 2009; Putnis & Timm, 2010). This would significantly decrease the potential for $^{40}$Ar escape from biotite and from relicts of MsA shielded from successive re-equilibration due to their microstructural position. On the other hand, the acquired porosity of muscovite of MsB composition, coupled with the fluid-driven dissolution–reprecipitation process as indicated by chemical heterogeneity, may have favoured the escape of $^{40}$Ar.

Several studies stress the importance of the availability of water for facilitating the resetting of the isotope record

(Berger, Wehrens, Lanari, Zwingmann, & Herwegh, 2017; Di Vincenzo et al., 2001; Villa, 2010). The range of $^{40}$Ar/$^{39}$Ar ages in sample to13-4 suggests that there was significant variability in fluid availability and permeability during the metamorphic cycle—otherwise all minerals should record a narrow range of exhumation-related ages following the thermal peak (Warren, Smye, et al., 2012). At the scale of the mineral assemblage, three successive fluid release events were responsible for successive muscovite chemical re-equilibration during the prograde path in sample to13-4 (Airaghi, Lanari, et al., 2017). Three intervals were also recognized in our geochronological data set for samples of the to13 series, defined by (1) the biotite core and MsA ages, (2) the biotite rims and MsB ages and (3) the MsC ages at *c.* 140–130 Ma. Mineral geochronometers might therefore be viewed as "geohygrometers" that essentially date fluid circulation episodes (often related to mineral re-equilibration events; Villa, 2010).

The chemical and geochronological heterogeneity of mica in different microstructural sites indicates that in our samples, the Ar record is mainly controlled by the rates of fluid-driven dissolution–reprecipitation processes rather than diffusion, as has been suggested in other lower grade metamorphic rocks (e.g. Cossette et al., 2015; Mulch & Cosca, 2004; Villa et al., 2014). The microstructural position of the grains might also be a key factor in explaining the different behaviour of Ar between muscovite and biotite.

While biotite (and garnet) indicate a precise and relatively limited part of the metamorphic path (prograde to peak amphibolite facies metamorphism at 220–180 Ma), the matrix muscovite seems to record a large part of the metamorphic history between 220 and 124 Ma (post peak-*P*), providing an age interval for each stage of the metamorphic path recorded in the chemistry of the mineral assemblage. Ages in the range of 150–124 Ma are therefore likely to represent the timing of a post peak-*T* metamorphic stage during decompression, down to the greenschist facies conditions.

## 8.3 | Regional tectonic implications

The allanite and biotite ages (200–170 Ma) are consistent with other data constraining the onset of the amphibolite facies metamorphism in the Danba area (~200 km southeastwards, Huang et al., 2003; Jolivet et al., 2015; Weller et al., 2013) and with muscovite $^{40}$Ar/$^{39}$Ar ages in the Northern Longmen Shan (Yan et al., 2011). Our ages are also in agreement with the time interval proposed for the emplacement of Mesozoic granites in the Songpan-Ganze region (de Sigoyer et al., 2014; Roger et al., 2004), which may mark the thermal peak in the westernmost Songpan-Ganze sedimentary series (Figure 11). In detail,

$^{40}$Ar/$^{39}$Ar ages in biotite record two stages of crystallization during amphibolite facies metamorphism (*c.* 220–200 Ma and *c.* 180 Ma), the timing of which is consistent with the age interval of the allanite analysed in this study (Figure 11).

On the basis of petrological observations, geochronological results and diffusion modelling, we relate the Late Triassic–Early Jurassic allanite and biotite ages to a medium-grade metamorphic event at amphibolite facies conditions in the Songpan-Ganze units of the central Longmen Shan syn- to post- the S2-forming phase of deformation. This medium-*T* metamorphic period lasted for over 20 Ma (Figure 11).

The allanite ages in the Tonghua massif may indicate that this slice of basement was already (marginally) affected by metamorphism (and deformation) during the Early Jurassic, although they might also be compatible with the upper limit of the time range indicated by the $^{40}$Ar/$^{39}$Ar muscovite ages. The $^{40}$Ar/$^{39}$Ar muscovite ages show indeed that the major reactivation of the massif occurred in the Early Cretaceous (Figure 11). The ages are unlikely to represent mixing ages between a Late Triassic–Early Jurassic (200–180 Ma) metamorphic event and a much younger Cenozoic event since first, there is no evidence of Cenozoic ages related to metamorphism in the central Longmen Shan, and second, the ages recorded in the sedimentary cover are also recorded in the Tonghua crystalline massif. Furthermore, Early Cretaceous ages were obtained also in the Pengguan crystalline massif (40 km southeastwards, Figure 11), where there is no evidence of Late Triassic–Early Jurassic metamorphism (Airaghi, Lanari, et al., 2017).
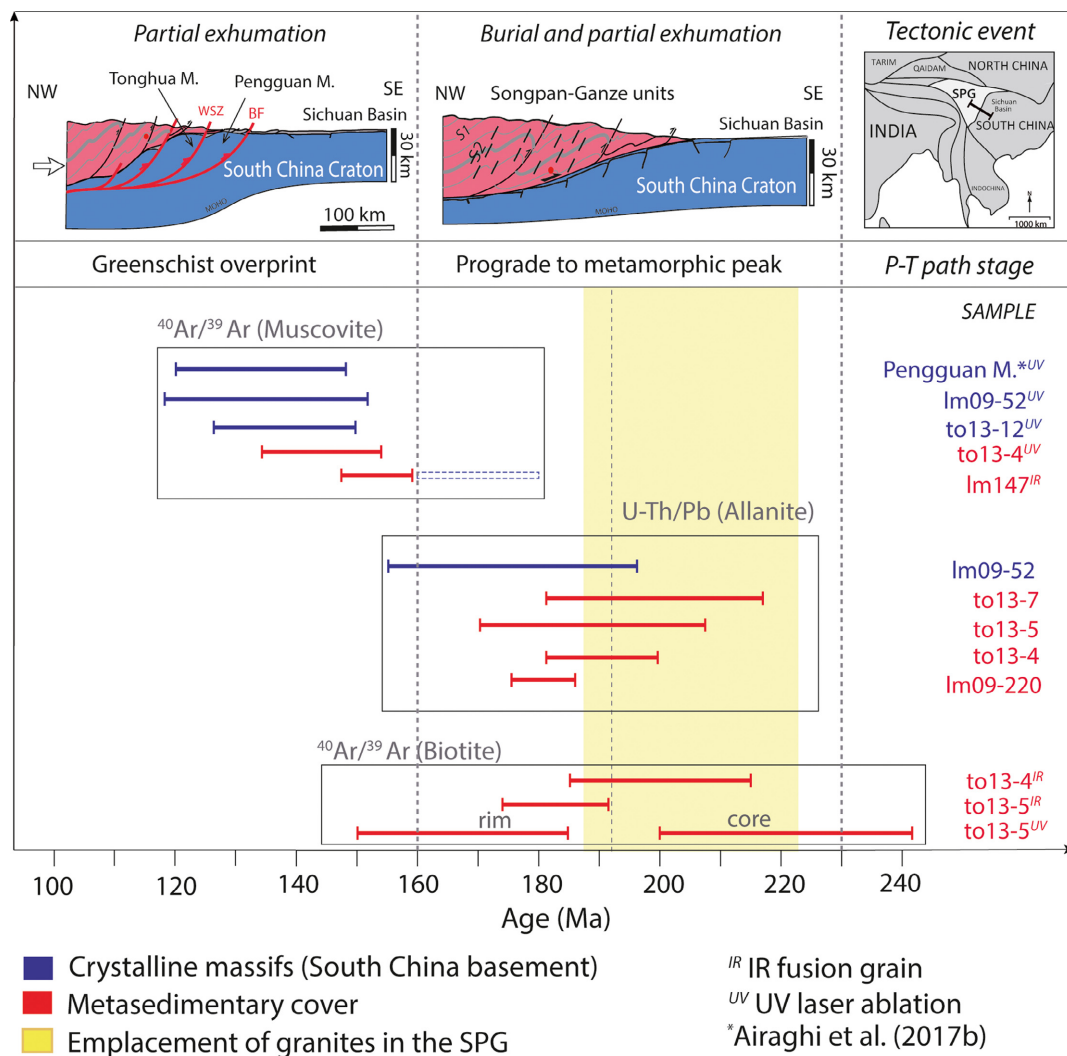


**FIGURE 11** Summary of in situ geochronological results and related metamorphic and tectonic events. * = age reported in Airaghi, de Sigoyer, et al. (2017) for the greenschist metamorphism in the Pengguan massif. Schematic cross-sections are modified from Airaghi, Lanari, et al. (2017). Red: metasedimentary cover. Blue: South China block (including the crystalline basement). The yellow frame indicates the time range for the emplacement of the Mesozoic granites (from de Sigoyer et al., 2014; Roger et al., 2004 and references therein)

In the internal metasedimentary cover, the occurrence of a greenschist facies event during the Early Cretaceous is consistent with the $^{40}Ar/^{39}Ar$ ages recorded in the Wenchuan fault zone (119–114 Ma, Arne et al., 1997) and with 123–120 Ma $^{40}Ar/^{39}Ar$ biotite ages from the Danba area (Xu et al., 2008). The Early Cretaceous also marks a change in the type and rate of sedimentation of the autochthonous units in the western Sichuan basin that become characteristic of a flexural basin forming in response to a rapid uplift of the belt (Liao, Hu, Zhang, Chen, & Sun, 2009). In order to explain the decreasing age of the Early Cretaceous event approaching the front of the belt, we propose that the related deformation phase firstly affected sediments in the northwest of the Tonghua area (lm147) at 160–147 Ma, and then propagated to the southeast at 150–135 Ma (to13-4), and to the basement in the Tonghua and Pengguan crystalline massifs at 140–118 Ma (lm09-52) and 145–130 Ma respectively (Figure 11).

Note that the Early Cretaceous phase is so far undocumented in the metamorphic evolution of the belt (except in the studies of Airaghi, de Sigoyer, et al., 2017) and marks the onset of thick-skinned deformation in the Longmen Shan. At this time, the internal units were already highly thickened (~30 km; Airaghi, Lanari, et al., 2017) and difficult to deform without propagating the deformation towards the front of the belt. Furthermore, our petrochronological results show that metasedimentary units in the internal part of the Longmen Shan were already partially exhumed by the Early Cretaceous, well before the Cenozoic exhumation phase.

The combination of petrological data with mica and allanite ages enables the first-order thermal history for the internal sedimentary units of the Longmen Shan to be documented, and associated with different phases of reactivation (Figure 12). The Early Cretaceous muscovite ages appear to be associated with a late greenschist overprint at ~320–400°C. The prograde path is constrained from petrology (Airaghi, Lanari, et al., 2017), while the $T$–$t$ estimates for the Miocene are derived from low-$T$ thermochronology (Godard et al., 2009; Kirby et al., 2002; Wang et al., 2012) and from previously published $^{40}Ar/^{39}Ar$ (Airaghi, de Sigoyer, et al., 2017). The cooling
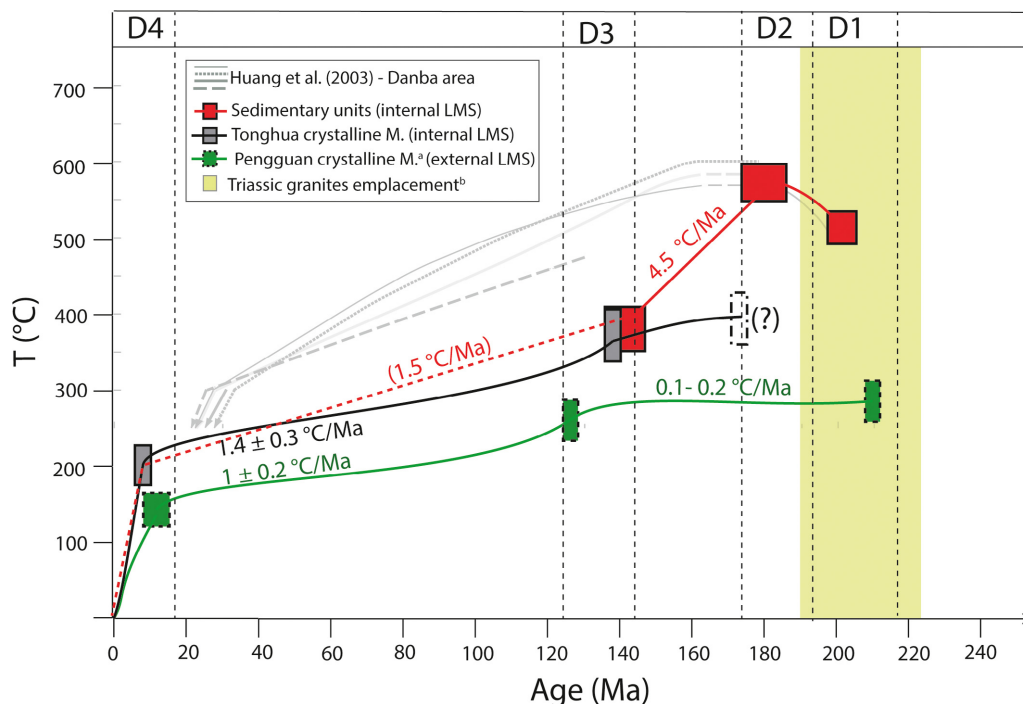


**FIGURE 12** Cooling histories for internal sedimentary units (red), internal Tonghua crystalline massif (black) and external crystalline Pengguan massif (green). Coloured rectangles represent the estimated temperature conditions at each stage (from petrology). Numbers between the squares are deduced cooling rates in °C/Ma. The red dashed cooling rate is the one that also appears in path B for Ar diffusion modelling. $T$–$t$ estimates for the Pengguan massif are from $^{40}Ar/^{39}Ar$ muscovite ages (Airaghi, de Sigoyer, et al., 2017); $T$–$t$ estimates for the Tonghua massif at 10 Ma are from zircon fission track (Tan et al., 2017); $T$–$t$ estimates for the Pengguan massif at <20 Ma are from zircon He ages (Godard et al., 2009). Grey lines are the cooling rates for the Danba units (~200 km southeast of the Longmen Shan) by Huang et al. (2003). Yellow frame: interval of granite emplacement in the Songpan-Ganze block (Roger et al., 2004). D1, D2 and D3 refer to the different deformation phases described in Section 3.2 and in Figure 2a. The timing of D4 is restrained to Cenozoic pulses of exhumation identified by low-$T$ thermochronology

path obtained for the internal sedimentary units (red in Figure 12) includes a relatively fast cooling rate of 4.5 ± 0.5°C/Ma from 580°C to ~400°C between 185 and 140 Ma (Early Cretaceous). This phase was followed by slower cooling at ~1.5°C/Ma until the Cenozoic exhumation phase at c. 20–10 Ma (Figure 12). The cooling rate of the internal Tonghua crystalline massif between 140 and 10 Ma was calculated at 1.4 ± 0.3°C/Ma by the integration of our geochronological results and recent zircon fission track ages revealing a rapid exhumation of the massif from ~200°C in the last 10 Ma (Tan et al., 2017).

In the Tonghua massif, the *P–T* data related to the Jurassic event are not precisely constrained. However, the absence of evidence for metamorphism higher than greenschist facies suggests that the Tonghua massif experienced conditions similar to those estimated for the Early Cretaceous event. The shape of cooling path of Figure 12 is similar to the one proposed for Danba region (grey lines in Figure 12; Huang et al., 2003), but in that area, the Early Cretaceous event remains unrecognized. We also observe a convergence of the thermal histories of the sedimentary units and crystalline massifs at 140–138 Ma. The basement and the sedimentary cover seem therefore to have experienced a coherent exhumation history since the Early Cretaceous reactivation. Prior to the Early Cretaceous, the crystalline massifs and the sedimentary cover experienced different thermal histories. The medium-grade metamorphic conditions recorded only in the metasedimentary cover at 200–180 Ma suggest indeed that it thickened independently from the basement. A major decollement between the sediments and the basement was therefore active during the Triassic–Early Jurassic.

Together these observations suggest that both the central Longmen Shan and the Danba region experienced a similar thermal evolution. In detail, the lower peak temperatures recorded in the studied area result in slower cooling rates during Cretaceous to Cenozoic times in the central Longmen Shan relative to the Danba area. The Early Cretaceous reactivation in the central Longmen Shan may be due to the far field effects of the collision between the Lhasa and Qiangtang blocks in the central Tibet, as suggested by Airaghi, de Sigoyer, et al. (2017 and references therein).

# 9 | CONCLUSIONS

This study demonstrates the complexity of interpreting $^{40}Ar/^{39}Ar$ ages of low- to medium-grade metamorphic rocks, especially for matrix phyllosilicates. The combination of petrological and geochronological results shows that in Longmen Shan, biotite porphyroblasts in amphibolite facies metapelites retain crystallization ages (i.e. ages that are consistent with U–Th/Pb allanite ages), despite experiencing relatively high temperatures (~580°C). Muscovite in the main foliation that re-equilibrated at the peak-*P*, peak-*T* and during the greenschist facies overprint instead records a more complex $^{40}Ar/^{39}Ar$ story. The muscovite $^{40}Ar/^{39}Ar$ ages comprise a mixture derived from the partial sampling of early MsA relics and a regionally consistent signal at c. 140–130 Ma. The difference between biotite and muscovite ages is not explainable by simple diffusion during protracted and slow cooling of grains of different size, as revealed by diffusion modelling experiments. Such a difference instead suggests successive recrystallization events. The microstructural position of muscovite in the main foliation as well as the acquired porosity during the previous metamorphic history may also have favoured the resetting of the Ar concentration in muscovite.

The combination of different petrological and geochronological methods provides an interpretative framework for the $^{40}Ar/^{39}Ar$ ages. Despite the fact that the in situ UV analyses could not resolve all the chemical heterogeneities due to their small size, the coupling with detailed petrological studies allowed the different generations of mica to be matched to their $^{40}Ar/^{39}Ar$ signature. In situ $^{40}Ar/^{39}Ar$ dating is a powerful technique that allows the entire metamorphic history to be traced by bracketing in time the different stages.

By using both Ar diffusion modelling and petrological observations, this study also tests all the hypotheses that may explain the $^{40}Ar/^{39}Ar$ ages. Here we show robust evidence for petrological and microstructural processes prevailing over thermally driven diffusion even at high temperatures. The complexity of the studied samples required significant underlying assumptions but the regional consistency of the data strengthen the geological interpretation of our results.

The $^{40}Ar/^{39}Ar$ biotite and U–Th/Pb allanite ages constrain the timing of medium-grade metamorphism in the sedimentary units in the central Longmen Shan (Tonghua area) to 220–180 Ma. The $^{40}Ar/^{39}Ar$ ages of muscovite in the S2 cleavage constrain the timing of the post-*T*-peak metamorphism up to the metamorphic overprint at greenschist facies conditions to 140–130 Ma. This event is also recorded in the crystalline Tonghua massif and is associated with deformation and a greenschist facies overprint at 7 ± 1 kbar, 370 ± 35°C. Our results show that metamorphism and deformation affected the sedimentary cover of the internal Longmen Shan (and maybe marginally the South China basement in the Tonghua crystalline massif) during the Late Triassic–Early Jurassic. This event was followed by a previously poorly recorded Early Cretaceous reactivation event that was responsible for the partial exhumation of the medium-grade metamorphic rocks and the crystalline massifs as a coherent system. This study

therefore shows that an important part of the crustal thickening and exhumation in eastern Tibet is inherited from the complex Mesozoic history, thus preceding the Cenozoic reactivation. The basement (in the crystalline massifs) was actively involved in the deformation since the Early Cretaceous.

## ORCID

*Laura Airaghi* ![iD] http://orcid.org/0000-0001-7032-2732

## REFERENCES

Airaghi, L., de Sigoyer, J., Lanari, P., Guillot, S., Vidal, O., Monié, P., ... Tan, X. (2017). Total exhumation across the Beichuan fault in the Longmen Shan (eastern Tibetan plateau, China): Constraints from petrology and thermobarometry. *Journal of Asian Earth Sciences*, 140, 108–121. https://doi.org/10.1016/j.jseaes.2017.04.003

Airaghi, L., Lanari, P., de Sigoyer, J., & Guillot, S. (2017). Microstructural vs compositional preservation and pseudomorphic replacement of muscovite in deformed metapelites from the Longmen Shan (Sichuan, China). *Lithos*, 282–283, 260–280.

Allaz, J., Engi, M., Berger, A., & Villa, I. M. (2011). The effects of retrograde reactions and diffusion on $^{40}$Ar-$^{39}$Ar ages of micas. *Journal of Petrology*, 52(4), 691–716. https://doi.org/10.1093/petrology/egq100

Arne, D., Worley, B., Wilson, C., Chen, S. F., Foster, D., Luo, Z. L., ... Dirks, P. (1997). Differential exhumation in response to episodic thrusting along the eastern margin of the Tibetan Plateau. *Tectonophysics*, 280, 239–256. https://doi.org/10.1016/S0040-1951(97)00040-1

Berger, A., Wehrens, P., Lanari, P., Zwingmann, H., & Herwegh, M. (2017). Microstructures, mineral chemistry and geochronology of white micas along a retrograde evolution: An example from the Aar massif (Central Alps, Switzerland). *Tectonophysics*, 721, 179–195. https://doi.org/10.1016/j.tecto.2017.09.019

Beyssac, O., Rouzaud, J. N., Goffé, B., Brunet, F., & Chopin, C. (2002). Graphitization in a high-pressure, low-temperature metamorphic gradient: A Raman microspectroscopy and HRTEM study. *Contributions to Mineralogy and Petrology*, 143, 19–31. https://doi.org/10.1007/s00410-001-0324-7

Billerot, A., Duchene, S., Vanderhaeghe, O., & de Sigoyer, J. (2017). Gneiss domes of the Danba Metamorphic Complex, Songpan Ganze, eastern Tibet. *Journal of Asian Earth Sciences*, 140, 48–74. https://doi.org/10.1016/j.jseaes.2017.03.006

Cenki-Tok, B., Darling, J. R., Rolland, Y., Dhuime, B., & Storey, C. D. (2014). Direct dating of mid-crustal shear zones with synkinematic allanite: New in situ U-Th-Pb geochronological approaches applied to the Mont Blanc massif. *Terra Nova*, 26(1), 29–37. https://doi.org/10.1111/ter.12066

Chen, S. F., & Wilson, C. (1995). Emplacement of the Longmen Shan thrust-nappe Belt along the eastern margin of the Tibetan Plateau. *Journal of Structural Geology*, 18, 413–430.

Cossette, E., Schneider, D. A., Warren, C. J., & Grasemann, B. (2015). Lithological, rheological, and fluid infiltration control on $^{40}$Ar/$^{39}$Ar ages in polydeformed rocks from the West Cycladic detachment system, Greece. *Lithosphere*, 7, 189–205. https://doi.org/10.1130/L416.1

de Sigoyer, J., Chavagnac, V., Blichert-Toft, J., Villa, I. M., Luais, B., Guillot, S., ... Mascle, G. (2000). Dating the Indian continental subduction and collisional thickening in the northwest Himalaya: Multichronology of the Tso Morari eclogites. *Geology*, 28(6), 487–490. https://doi.org/10.1130/0091-7613(2000)28&lt;487:DTICSA&gt;2.0.CO;2

de Sigoyer, J., Vanderhaeghe, O., Duchene, S., & Billerot, A. (2014). Generation and emplacement of Triassic granitoids within the Sonpan Ganze accretionary orogenic wedge in a context of slab retreat accommodated by tear faulting, Eastern Tibetan plateau, China. *Journal of Asian Earth Sciences*, 88, 192–216. https://doi.org/10.1016/j.jseaes.2014.01.010

Di Vincenzo, G., Ghiribelli, B., Giorgetti, G., & Palmeri, R. (2001). Evidence of a close link between petrology and isotope records: Constraints from SEM, EMP, TEM and in situ $^{40}$Ar-$^{39}$Ar laser analyses on multiple generations of white micas (Lanterman Range, Antarctica). *Earth and Planetary Science Letters*, 192, 389–405. https://doi.org/10.1016/S0012-821X(01)00454-X

Dirks, P. H. G. M., Wilson, C. J. L., Chen, S., Luo, Z. L., & Liu, S. (1994). Tectonic evolution of the NE margin of the Tibetan Plateau; evidence from central Longmen Mountains, Sichuan Province, China. *Journal of Southeast Asian Earth Sciences*, 9, 181–192. https://doi.org/10.1016/0743-9547(94)90074-4

Dodson, M. H. (1973). Closure temperature in cooling geochronological and petrological systems. *Contributions to Mineralogy and Petrology*, 40, 259–274. https://doi.org/10.1007/BF00373790

Dubacq, B., Vidal, O., & De Andrade, V. (2010). Dehydration of dioctahedral aluminous phyllosilicates: Thermodynamic modelling and implications for thermobarometric estimates. *Contributions to Mineralogy and Petrology*, 159, 159–174. https://doi.org/10.1007/s00410-009-0421-6

Fornash, K. F., Cosca, M. A., & Whitney, D. L. (2016). Tracking the timing of subduction and exhumation using $^{40}$Ar/$^{39}$Ar phengite ages in blueschist- and eclogite-facies rocks (Sivrihisar, Turkey). *Contributions to Mineralogy and Petrology*, 171(7), 67. https://doi.org/10.1007/s00410-016-1268-2

Godard, V., Pik, R., Lav, J., Cattin, R., Tibari, B., de Sigoyer, J., ... Zhu, J. (2009). Late Cenozoic evolution of the central Longmen Shan, eastern Tibet: Insight from (U-Th)/He thermochronometry. *Tectonics*, 28, TC5009.

Hames, W. E., & Browring, S. A. (1994). An empirical evaluation of the argon diffusion geometry in muscovite. *Earth and Planetary Science Letters*, *124*(1), 161–169. https://doi.org/10.1016/0012-821X(94)00079-4

Hames, W. E., & Cheney, J. T. (1997). On the loss of $^{40}$Ar* from muscovite during polymetamorphism. *Geochimica et Cosmochimica Acta*, *61*, 3863–3872. https://doi.org/10.1016/S0016-7037(97)00207-X

Harrison, T. M., Célérier, J., Aikman, A. B., Hermann, J., & Hizler, M. T. (2009). Diffusion of $^{40}$Ar in muscovite. *Geochimica et Cosmochimica Acta*, *73*, 1039–1051. https://doi.org/10.1016/j.gca.2008.09.038

Harrison, T. M., Duncan, I., & McDougall, I. (1985). Diffusion of $^{40}$Ar in biotite: Temperature, pressure and compositional effects. *Geochimica et Cosmochimica Acta*, *49*, 2461–2468. https://doi.org/10.1016/0016-7037(85)90246-7

Harrowfield, M. J., & Wilson, C. J. L. (2005). Indosinian deformation of the Songpan Garzë Fold Belt, northeast Tibetan Plateau. *Journal of Structural Geology*, *27*, 101–117. https://doi.org/10.1016/j.jsg.2004.06.010

Hermann, J., & Rubatto, D. (2003). Relating zircon and monazite domains to garnet growth zones: Age and duration of granulite facies metamorphism in the Val Malenco lower crust. *Journal of Metamorphic Geology*, *21*(9), 833–852. https://doi.org/10.1046/j.1525-1314.2003.00484.x

Holdaway, M. J., & Lee, S. M. (1977). Fe-Mg cordierite stability in high grade politic rocks based on experimental, theoretical and natural observations. *Contributions to Mineralogy and Petrology*, *63*, 175–198. https://doi.org/10.1007/BF00398778

Huang, M., Maas, R., Buick, I. S., & Williams, I. S. (2003). Crustal response to continental collision between the Tibet, Indian, South China and North China Blocks: Geochronological constraints from the Songpan-Garzê Orogenic Belt, western China. *Journal of Metamorphic Geology*, *21*, 223–240. https://doi.org/10.1046/j.1525-1314.2003.00438.x

Janots, E., Engi, M., Rubatto, D., Berger, A., Gregory, C., & Rahn, M. (2009). Metamorphic rates in collisional orogeny from in situ allanite and monazite dating. *Geology*, *37*(1), 11–14. https://doi.org/10.1130/G25192A.1

Janots, E., & Rubatto, D. (2014). U-Th-Pb dating of collision in the external Alpine domains (Urseren zone, Switzerland) using low temperature allanite and monazite. *Lithos*, *184*, 155–166. https://doi.org/10.1016/j.lithos.2013.10.036

Jolivet, M., Roger, F., Xu, Z. Q., Paquette, J.-L., & Cao, H. (2015). Mesozoic-Cenozoic evolution of the Danba dome (Songpan Garzê, East Tibet) as inferred from LA-ICPMS U-Pb and fission-track data. *Journal of Asian Earth Sciences*, *102*, 180–204. https://doi.org/10.1016/j.jseaes.2015.02.009

Kelley, S. (1988). The relationship between K-Ar mineral ages, mica grainsize and movement on the Moine Thrust Zone, NW Highlands, Scotland. *Journal of the Geological Society*, *145*, 1–10. https://doi.org/10.1144/gsjgs.145.1.0001

Kirby, E., Reiners, P., Krol, M., Hodges, K., Whipple, K., Farley, K., . . . Chen, Z. (2002). Late Cenozoic uplift and landscape evolution along the eastern margin of the Tibetan Plateau: Inferences from $^{40}$Ar/$^{39}$Ar and (U-Th)/He thermochronology. *Tectonics*, *21*(1), 1001.

Kramar, N., Cosca, M. A., & Hunziker, J. C. (2001). Heterogeneous 40Ar* distributions in naturally deformed muscovite: In situ UV-laser ablation evidence for microstructurally controlled intragrain diffusion. *Earth and Planetary Science Letters*, *192*(3), 377–388. https://doi.org/10.1016/S0012-821X(01)00456-3

Lanari, P., Guillot, S., Schwartz, S., Vidal, O., Tricart, P., Riel, N., . . . Beyssac, O. (2012). Diachronous evolution of the alpine continental subduction wedge: Evidence from P-T estimates in the Briannonais Zone houillère (France - Western Alps). *Journal of Geodynamics*, *56–57*, 39–54. https://doi.org/10.1016/j.jog.2011.09.006

Lanari, P., Riel, N., Guillot, S., Vidal, O., Schwartz, S., Pêcher, A., . . . Hattori, K. (2013). Deciphering high-pressure metamorphism in collisional context using microprobe mapping methods: Application to the Stak eclogitic massif (northwest Himalaya). *Geology*, *41*, 11–114.

Lanari, P., Rolland, Y., Schwartz, S., Vidal, O., Guillot, S., Tricart, P., . . . Dumont, T. (2014). P–T–t estimation of deformation in low-grade quartz-feldspar-bearing rocks using thermodynamic modelling and $^{40}$Ar/$^{39}$Ar dating techniques: Example of the Plan-de-Phasy shear zone unit (Briançonnais Zone, Western Alps). *Terra Nova*, *26*(2), 130–138. https://doi.org/10.1111/ter.12079

Lanari, P., Vidal, O., De Andrade, V., Dubacq, B., Lewin, E., Grosch, E., . . . Schwartz, S. (2014). XMapTools: A MATLAB-based program for electron microprobe X-ray image processing and geothermobarometry. *Computers & Geosciences*, *62*, 227–240. https://doi.org/10.1016/j.cageo.2013.08.010

Li, S., Currie, B. S., Rowley, D. B., & Ingalls, M. (2015). Cenozoic paleoaltimetry of the SE margin of the Tibetan Plateau: Constraints on the tectonic evolution of the region. *Earth and Planetary Science Letters*, *432*, 415–424. https://doi.org/10.1016/j.epsl.2015.09.044

Li, Z.-W., Liu, S., Chen, H., Deng, B., Hou, M., Wu, W., . . . Cao, J. (2012). Spatial variation in Meso-Cenozoic exhumation history of the Longmen Shan thrust belt (eastern Tibetan Plateau) and adjacent western Sichuan basin: Constraints from fission track thermochronology. *Journal of Asian Earth Sciences*, *47*, 185–203. https://doi.org/10.1016/j.jseaes.2011.10.016

Liao, T., Hu, J., Zhang, F., Chen, H., & Sun, H. (2009). Relation between structural evolution of the Longmenshan orogenic zone and sedimentation of its foreland basin. *Mining Science and Technology (China)*, *19*(6), 807–812. https://doi.org/10.1016/S1674-5264(09)60147-2

McDonald, C., Warren, C. J., Mark, D. F., Halton, A. M., Kelley, S. P., & Sherlock, S. C. (2016). Argon redistribution during a metamorphic cycle: Consequences for determine cooling rates. *Chemical Geology*, *443*, 182–197. https://doi.org/10.1016/j.chemgeo.2016.09.028

Mottram, C., Warren, C. J., Halton, A. M., Kelley, S. P., & Harris, N. B. W. (2015). Argon behavior in an inverted Barrovian sequence, Sikkim Himalaya: The consequences of temperature and timescale on $^{40}$Ar/$^{39}$AR mica geochronology. *Lithos*, *238*, 37–51. https://doi.org/10.1016/j.lithos.2015.08.018

Mulch, A., & Cosca, M. A. (2004). Recrystallization or cooling ages: *In situ* UV-laser $^{40}$Ar/$^{39}$Ar geochronology of muscovite in mylonitic rocks. *Journal of the Geological Society, London*, *161*, 573–582. https://doi.org/10.1144/0016-764903-110

Mulch, A., Cosca, M. A., Andersen, A., & Fiebig, J. (2005). Time scales of deformation and exhumation in extensional detachment systems determined by high-spatial resolution in situ UV-laser $^{40}$Ar/$^{39}$Ar dating. *Earth and Planetary Science Letters*, *233*, 375–390. https://doi.org/10.1016/j.epsl.2005.01.042

Mulch, A., Cosca, M. A., & Handy, M. R. (2002). In-situ UV-laser $^{40}Ar/^{39}Ar$ geochronology of a micaceous mylonite: An example of defect-enhanced argon loss. *Contributions to Mineralogy and Petrology*, *142*, 738–752. https://doi.org/10.1007/s00410-001-0325-6

Perchuk, L. L., & Lavrent'eva, I. V. (1983). Experimental investigation of exchange equilibria in the system cordierite-garnet-biotite. *Kinetics and Equilibrium in Mineral Reactions*, *3*, 199–239. https://doi.org/10.1007/978-1-4612-5587-1

Putnis, A. (2009). Mineral replacement reactions. In E. H. Oelkers & J. Schott (Eds.), Thermodynamics and kinetics of water-rock interactions. *Reviews in Mineralogy & Geochemistry*, *70*, 87–124.

Putnis, A., & Timm, J. (2010). Replacement processes in the Earth's crust. *Elements*, *6*(3), 159–164. https://doi.org/10.2113/gselements.6.3.159

Richardson, N. J., Densmore, A. L., Seward, D., Fowler, A., Wipf, M., Ellis, M. A., . . . Zhang, Y. (2008). Extraordinary denudation in the Sichuan Basin: Insights from low-temperature thermochronology adjacent to the eastern margin of the Tibetan Plateau. *Journal of Geophysical Research*, *113*, B04409.

Roger, F., Jolivet, M., Cattin, R., & Malavieille, J. (2011). Mesozoic-Cenozoic tectonothermal evolution of the eastern part of the Tibetan Plateau (Songpan-Ganze, Longmen Shan area): Insights from thermochronological data and simple thermal modelling. *Geological Society of London, Special Publications*, *353*, 9–25. https://doi.org/10.1144/SP353.2

Roger, F., Jolivet, M., & Malavieille, J. (2010). The tectonic evolution of the Songpan-Garze (North Tibet) and adjacent areas from Proterozoic to Present: A synthesis. *Journal of Asian Earth Sciences*, *39*, 254–269. https://doi.org/10.1016/j.jseaes.2010.03.008

Roger, F., Malavieille, J., Leloup, Ph. H., Calassou, S., & Xu, Z. (2004). Timing of granite emplacement and cooling in the Songpan-Garzê Fold Belt (eastern Tibetan Plateau) with tectonic implications. *Journal of Asian Earth Sciences*, *22*, 465–481. https://doi.org/10.1016/S1367-9120(03)00089-0

Rolland, Y., Sosson, M., Adamia, S., & Sadradze, N. (2011). Prolonged Variascan to Alpine history of an active Eurasian margin (Georgia, Armenia) revealed by $^{40}Ar/^{39}Ar$ dating. *Gondwana Research*, *20*, 798–815. https://doi.org/10.1016/j.gr.2011.05.007

Sanchez, G., Rolland, Y., Schneider, J., Corsini, M., Oliot, E., Goncalves, P., . . . Marquer, D. (2011). Dating low-temperature deformation by $^{40}Ar/^{39}Ar$ on white mica, insights from the Argentera-Mercantour Massif (SW Alps). *Lithos*, *125*, 521–536. https://doi.org/10.1016/j.lithos.2011.03.009

Scheffer, C., Vanderhaeghe, O., Lanari, P., Tarantola, A., Ponthus, L., Photiades, A., . . . France, L. (2016). Syn- to post-orogenic exhumation of metamorphic nappes: Structure and thermobarometry of the western Attic-Cycladic metamorphic complex (Lavrion, Greece). *Journal of Geodynamics*, *96*, 174–193. https://doi.org/10.1016/j.jog.2015.08.005

Spear, F. S., & Parrish, R. R. (1996). Petrology and cooling rates of the Valhalla Complex, British Columbia, Canada. *Journal of Petrology*, *37*(4), 733–765. https://doi.org/10.1093/petrology/37.4.733

Stacey, J. S., & Kramers, J. D. (1975). Approximation of terrestrial lead isotope evolution by a two-stage model. *Earth and Planetary Science Letters*, *26*, 207–221. https://doi.org/10.1016/0012-821X(75)90088-6

Stübner, K., Warren, C., Ratschbacher, L., Sperner, B., Kleeberg, R., Pfänder, J., . . . Grujic, D. (2017). Anomalously old biotite

$^{40}Ar/^{39}Ar$ ages in the NW Himalaya. *Lithosphere*, *9*(3), 366–383. https://doi.org/10.1130/L586.1

Tan, X., Lee, Y.-H., Xu, X.-W., & Cook, K. L. (2017). Cenozoic exhumation of the Danba antiform, eastern Tibet: Evidence from low-temperature thermochronology. *Lithosphere*, *9*(4), 534–544.

Tera, F., & Wasserburg, G. J. (1972). U-Th-Pb systematics in lunar highland samples from the Luna 20 and Apollo 16 missions. *Earth and Planetary Science Letters*, *17*, 36–51. https://doi.org/10.1016/0012-821X(72)90257-9

Thompson, A. B. (1976). Mineral reactions in pelitic rocks: I. Prediction of P-T–X (Fe–Mg) phase relations. *American Journal of Science*, *276*, 401–424. https://doi.org/10.2475/ajs.276.4.401

Villa, I. M. (1998). Isotopic closure. *Terra Nova*, *10*, 42–47. https://doi.org/10.1046/j.1365-3121.1998.00156.x

Villa, I. M. (2010). Disequilibrium textures versus equilibrium modelling: Geochronology at the crossroads. *Geological Society, London, Special Publications*, *332*, 1–15. https://doi.org/10.1144/SP332.1

Villa, I. M. (2015). $^{39}Ar-^{40}Ar$ geochronology of mono- and polymetamorphic basement rocks. *Periodico di Mineralogia*, *84*(3B), 615–632.

Villa, I. M. (2016). Diffusion in mineral geochronometers: Present and absent. *Chemical Geology*, *420*, 1–10. https://doi.org/10.1016/j.chemgeo.2015.11.001

Villa, I. M., Bucher, S., Bousquet, R., Kleinhanns, I. C., & Schmid, S. M. (2014). Dating polygenetic metamorphic assemblages along a transect across the Western Alps. *Journal of Petrology*, *55*(4), 803–830. https://doi.org/10.1093/petrology/egu007

Wang, E., Kirby, E., Furlong, K., van Soest, M., Xu, G., Shi, X., . . . Hodges, K. (2012). Two-phase growth of high topography in eastern Tibet during the Cenozoic. *Nature Geoscience*, *5*, 640–645. https://doi.org/10.1038/ngeo1538

Warren, C. J., Hanke, F., & Kelley, S. P. (2012). When can muscovite $^{40}Ar/^{39}Ar$ dating constrain the timing of metamorphic exhumation? *Chemical Geology*, *291*, 79–86. https://doi.org/10.1016/j.chemgeo.2011.09.017

Warren, C. J., Sherlock, S. C., & Kelley, S. P. (2011). Interpreting high-pressure phengite $^{40}Ar/^{39}Ar$ laserprobe ages: An example from Saih Hatat, NE Oman. *Contributions to Mineralogy and Petrology*, *161*, 991–1009. https://doi.org/10.1007/s00410-010-0576-1

Warren, C. J., Smye, A. J., Kelley, S. P., & Sherlock, S. C. (2012). Using $^{40}Ar/^{39}Ar$ data as a tracer for fluid flow and permeability under high-*P* conditions: Tauern Window, Eastern Alps. *Journal of Metamorphic Geology*, *30*, 63–80. https://doi.org/10.1111/j.1525-1314.2011.00956.x

Weller, O. M., St-Onge, M. R., Waters, D. J., Rayner, N., Searle, M. P., Chung, S.-L., . . . Xu, X. (2013). Quantifying Barrovian metamorphism in the Danba Structural Culmination of eastern Tibet. *Journal of Metamorphic Geology*, *31*(9), 909–935. https://doi.org/10.1111/jmg.12050

Wheeler, J. (1996). DIFFARG: A program for simulating argon diffusion profiles in minerals. *Computers & Geosciences*, *22*(8), 919–929. https://doi.org/10.1016/S0098-3004(96)00061-1

Whitney, D. L., & Bernard, W. E. (2010). Abbreviations for names of rock-forming minerals. *American Mineralogist*, *95*, 185–187.

Worley, B. A., & Wilson, C. J. L. (1996). Deformation partitioning and foliation reactivation during transpressional orogenesis, an example from the Central Longmen Shan, China. *Journal of Structural Geology*, *18*, 395–411. https://doi.org/10.1016/0191-8141(95)00095-U

Xu, Z., Ji, S., Li, H., Hou, L., Fu, X., & Cai, Z. (2008). Uplift of the Longmen Shan range and the Wenchuan earthquake. *Journal of International Geosciences, Episodes*, *31*, 291–301.

Yan, D.-P., Zhou, M.-F., Li, S.-B., & Wei, G.-Q. (2011). Structural and geochronological constrains on the Mesozoic-Cenozoic evolution of the Longmen Shan thrust belt, eastern Tibetan Plateau. *Tectonics*, *30*, TC6005.

Yan, D., Zhou, M., Wei, G., Gao, J., Liu, S., Xu, P., ... Shi, X. (2008). The Pengguan tectonic dome of Longmen Mountains, Sichuan Province: Mesozoic denudation of Neoproterozoic magmatic arc-basin system. *Science in China Series D-Earth Sciences*, *51*, 1545–1559. https://doi.org/10.1007/s11430-008-0126-0

Zhou, M.-F., Yan, D.-P., Wang, C.-L., Qi, L., & Kennedy, A. (2006). Subduction-related origin of the 750 Ma Xuelongbao adakitic complex (Sichuan Province, China): Implications for the tectonic setting of the giant Neoproterozoic magmatic event in South China. *Earth and Planetary Science Letters*, *248*, 271–285.

## SUPPORTING INFORMATION

Additional supporting information may be found online in the Supporting Information section at the end of the article.

**Appendix S1.** Analytical methods for geochronology.

**Figure S1.** Compositional X-ray maps of allanite of metapelites to13-4 and to13-7.

**Figure S2.** Thermobarometric estimates for samples lm09-52 and lm09-53 from the Tonghua crystalline massif obtained with the white mica-chlorite-quartz multi-equilibrium approach.

**Table S1.** Chemical analyses for allanite of two representative metapelites: samples to13-5 and to13-4.

**Table S2.** Ar data for all analyzed samples.